The technical report for

Passive acoustic technique for detecting, locating, and characterizing hydrocarbon leakages

The Gulf Research Program of the National Academy of Science

Grant Award Number: 200008860

Zhiqu Lu[a,b], Xudong Fan[b], Xing Yang[c] , Raviteja Chinnambetib[c], Likun Zhang[b], and Lei Cao[c],

[a]National Center for Physical Acoustics, The University of Mississippi, University, MS

[b]The Department of Physics & Astronomy, The University of Mississippi

[c]The Department of Electrical Engineering, The University of Mississippi

Table of content

1. Project Summary

In this project, the National Center for Physical Acoustics, collaborating with the Department of Physics and the Department of Electrical Engineering at the University of Mississippi has developed a hydrophone network-based real-time passive monitoring system for detecting, locating, and characterizing hydrocarbon leakages undersea. This project directly addresses the purpose of reducing the systemic risks leading to uncontrolled hydrocarbon release set by the Gulf Research Program.

The U.S. outer continental shelf is a major source of energy for the United States. The rapid growth of oil and gas production in the Gulf of Mexico increases the risk of underwater oil spills at greater water depths and drilling wells. These hydrocarbons leakages can be caused by either natural events, such as seeping from fissures in the ocean seabed, or by anthropogenic accidents, such as leaking from broken wellheads and pipelines. In order to improve safety and reduce the environmental risks of offshore oil and gas operations, the Bureau of Safety and Environmental Enforcement recommended the use of real-time monitoring. An early warning system for detecting, locating, and characterizing hydrocarbon leakages is essential for preventing the next oil spill as well as for seafloor hydrocarbon seepage detection. Existing techniques, such as an acoustic array apparatus, hydrostatic pressure tests, and acoustic sonars, either cannot determine the exact location or need to be deployed in a close range of the leakage location.

With the goal of leakage detection and localization, our approach consists of recording and modeling the acoustic signals induced by the oil-spill and implementing advanced signal processing and triangulation localization techniques with a hydrophone network. In an oil spill event, the leaked hydrocarbon is injected into seawater with huge amounts of discharge at high speeds. With mixed natural gases and oils, this hydrocarbon leakage creates underwater sound through two major mechanisms: shearing and turbulence by a streaming jet of oil droplets and gas bubbles, and bubble oscillation and collapse. These acoustic emissions can be recorded by hydrophones in the water column at far distances. They will be characterized and differentiated from other underwater noises through their unique frequency spectrum, evolution and transportation processes and recording positions, and further be utilized to detect and position the leakage locations.

Tasks of this project are:

1. Conduct a laboratory study to simulate hydrocarbon leakages and their induced sound under controlled conditions, and to establish the correlation between frequency spectra and leakage properties, such as oil-jet intensities and speeds, bubble radii and distributions, and crack sizes.
2. Implement and develop acoustic bubble modeling for estimating features and strength of the oil leakage.
3. Develop a set of advanced signal processing and triangulation algorithms for leakage detection and localization.

2. Research Objectives and Goals

The U.S. outer continental shelf is a major source of energy for the United States. The rapid growth of oil and gas production in the Gulf of Mexico increases the risk of underwater oil spills at greater water depths and at drilling wells, where crude oils/hydrocarbons are under high pressure and temperature conditions. These hydrocarbon leakages can be caused by either natural events, such as seeping from fissures in the ocean seabed and eroding sedimentary rock (http://www.soscalifornia.org/natural-oil-seepage-facts/), or by anthropogenic accidents, such as leaking from broken wellheads and pipelines by mechanical failures - like the Macondo well blowout and Deepwater Horizon mobile offshore drilling unit explosion in April 2010 (Deepwater Horizon Study Group, 2011). The consequence of the leakages can be extensive damage to marine environment, beaches, wetlands , estuaries, marine and wildlife habitats, and fishing and tourism industries (Tangley, 2010; Juhasz, 2012). In order to improve safety and reduce environmental risks of offshore oil and gas operations, the Bureau of Safety and Environmental Enforcement (BSEE) of the U.S. Department of the Interior recommended the use of real-time monitoring (Transportation Research Board Special Report 322, 2016). An early warning system for detecting, locating, and characterizing hydrocarbon leakages is essential for preventing the next spill as well as for seafloor hydrocarbon seepage detection.

Existing methods for oil pipeline leak detection, such as an acoustic array apparatus (US patent # US20170002642) and hydrostatic tests (https://en.wikipedia.org/wiki/Hydrostatic_test#Pipeline_testing), generally concern the detection of cracks and pressure abnormalities inside the pipeline system. While deploying contact sensors along the oil transportation system, these methods still may not provide the exact position when a leakage occurs. Active acoustic methods for oil leak investigation were reported using acoustic backscatter (Lorio, 2017), acoustic imaging sonar, and Doppler sonar (Camilli, et al., 2012). These active acoustic techniques used highly-directional narrow beam acoustic sources at frequencies ranging from several hundred kHz to several MHz, and thereby required the acoustic devices to be positioned at close range to an oil plume. For example, horizontal standoff distances of between 2 m and 7 m were reported (Camilli, et al., 2012). The active measurements also require an operational vessel to transport these expensive acoustic instruments to a known oil leak area within a limited period of time. All of these techniques have their technical limitations and cannot achieve all the functions for a real-time monitoring system.

In this project, the National Center for Physical Acoustics (NCPA), collaborating with the Department of Physics and the Department of Electrical Engineering at the University of Mississippi (UM), launched an integrated study to develop a hydrophone network-based real-time passive monitoring system for detecting, locating, and characterizing hydrocarbon leakages. So far, direct research on real-time monitoring and localization technology via passive acoustic techniques has not been implemented. As compared with the active acoustic techniques, the passive acoustic method can cover large areas and achieve long-term monitoring in a cost-effective manner. The methodology in this project exploits the advantages of both oil spill-induced underwater sound physics and underwater acoustic sensing techniques, along with an advanced localization technique, as described below.

In an oil spill event, the leaked hydrocarbon is injected into seawater with huge amounts of discharge - for example, an estimated 4.9 million barrels in the DWH oil spill (United States Coast Guard, National Response Teams (U.S.), 2011). This discharge can extend over a long period of time and at high speeds that vary depending on the sizes and depths of the leakages. The spilled crude oil is a mixture of natural gases and oils with considerable amounts of gases (a reported gas-to-oil ratio of 1,600 ft^3/bbl, Reddya, et al., 2012). This hydrocarbon leakage usually undergoes two transporting processes: (1) a buoyant jet stage of oil droplets and gas bubbles near the leakage point with high speeds and (2) an advection diffusion stage as oil droplets and gas bubbles move far away from the leakage point and form rising and transporting plumes at relatively slow speeds (Niu, et al., 2013). During the jet stage, both oil and bubbles with exiting

momentum interact with surrounding seawater to create turbulence and shearing. The turbulence and shearing effects can generate underwater noise, similar to wind noise generation mechanisms for infrasound (Abbott and Raspet, 2015). Meanwhile, the gas bubbles experience dramatic shape deformation due to sudden changes in hydrostatic pressure and jet velocity, which triggers the oscillation of gas bubbles and initiates the generation of bubble sounds (Leighton, 1994). During the advection and diffusion stage, the rising bubbles continue to oscillate and collapse, but undergo slow evolutions due to the variations in hydrostatic pressure and temperature - which results in variations of diameter and density of the gas bubbles (Leighton, 1994; Wilcock, et al., 2014; Riccardi and Bernardis, 2016). The oil plume with bubble cluster undergoes transport processes due to ocean currents and gravitational effects. The bubble-induced underwater sounds in this stage exhibit a temporally and spatially varied frequency spectrum. Therefore, the oil spill sounds can be differentiated from other underwater noises through their unique frequency spectra and temporal evolution and spatial transportation processes (Urick, 1983; Leighton, 1994; Lurton, 2002).

These oil spill-induced underwater acoustic emissions can be recorded by omnidirectional hydrophones in the water column at far distances due to low attenuation in seawater (Urick, 1983; Lurton, 2002). They can be analyzed and characterized to provide information regarding the early stage, extent, and location of the leakages. In a real-time monitoring system, a hydrophone network can be anchored permanently in the water column far away from the sea surface and close to the seafloor or wellhead, thus effectively suppressing the interferences of surface noises caused by winds, waves, rains, shipping, and industrial activities (Urick, 1983; Lurton, 2002).

Development of a real-time hydrophone monitoring system for practical leakage detection and location will require a fundamental understanding of: (1) the relationship between the acoustic responses and oil spill properties (such as oil-jet intensities and velocities, bubble radius and distributions, and crack sizes); and (2) hydrocarbon leakage-induced underwater sound. To achieve these goals, laboratory experiments under controlled conditions have been conducted.

We have implemented acoustic bubble modeling (Leighton and Walton, 1987) for estimating features and strength of the oil leakage from the sound recorded by hydrophones and from the determined range/distance of the leakage site. The modeling will estimate bubble concentration/population histograms showing the number of bubbles excited in a given size range at the leakage as well as sound strength. For this purpose, we will implement modeling for the passive acoustic emissions of freely-oscillating bubbles and/or develop modeling for bubble clusters in the specific context/type of oil leakage. The proper implementation and/or development of the modeling will rely on results gained from the laboratory data.

Using a hydrophone network, a triangulation localization method will be developed and applied to determine the leak location. Localization techniques have been extensively studied and developed in wireless communications. In Global Positioning System (GPS)-based navigation applications, a GPS receiver can use signals broadcasted from four satellites to identify its three-dimensional location (Blewitt, 1997). For mission emergency and public safety, cellular systems can also use received signals from different base stations to locate a specific mobile user. With the development of sensor networks, underwater localization (Tan et. al., 2011; Ribeiro et. al., 2015; Erol-Kantarci, 2011) has become increasingly important to support various civilian and military applications. These localization methods are generally based on one or a group of triangulation techniques that utilize signals including received signal strength (RSS), time-of-arrival (TOA), time difference-of-arrival (TDOA), and angle-of-arrival (AOA). In oil-leakage detection, since the hydrophones do not have prior knowledge of leakages (such as the emitting time and strength of the sound signal), TDOA will be exploited to design localization algorithms.

Exploiting the advantages of both underwater acoustic sensing techniques and oil spill-induced underwater sound mechanisms, along with an advanced localization technique, our study directly address the issues

requested by the Gulf Research Program in Preventing the Next Spill: Understanding Systemic Risk in the Oil and Gas Environment: for seafloor hydrocarbon detection technology.

Specific tasks of the research were:

1. Conduct a laboratory study to simulate hydrocarbon leakage under controlled conditions (pressures, flow rates, opening sizes, and types of leakages), to record the oil leakage-induced underwater sound, and to establish the correlation between frequency spectra and oil leakage properties, such as oil-jet intensities and velocities, bubble radii and distributions, and crack sizes.
2. Implement and develop acoustic bubble modeling for understanding and estimating properties of the oil leakage
3. Develop a set of signal processing and triangulation algorithms for leakage identification and localization.

3. Laboratory Oil Spill Experiments.

3.1 Experimental setup

For **Task 1**, the experimental setup consisted of a water tank, two bubble sources, two active hydrophone sources, a passive hydrophone network, five passive hydrophone arrays, an instrument control and data acquisition system, and an underwater camera.

The dimensions of the water tank were 2.13 m×2.13 m×1.83 m (7'×7'×6'). This rectangular tank was filled with tap water to a water level of 1.68 m.

In the study, two types of oil leakages were investigated: (1) a few bubble case to simulate oil seepage from fissures in the ocean seabed, and (2) a constant flow case to simulate gas leakage from broken wellheads or pipelines. For creating the two types of oil leakage in a controllable manner, a bubble generation system was built. A schematic diagram of the system is shown in Fig. 3.1. For a few bubble case, a syringe pump (WPI, SP260P) was used as a small volume gas reservoir. The pump was flow rate controllable and programmed by a computer via RS232-2 interface and the gas under test was pushed by the syringe pump into the transport gas line at very low flow rates in order to generate a single bubble or a few bubbles. For the constant flow bubble case, a compressed gas (either nitrogen or methane gases) cylinder served as a large volume gas reservoir to introduce continuous gas at a constant flow rate into the gas line. A pressure regulator/gauge adjusted manually the output pressure of the gas. A 3-way valve was employed to switch the connections among the syringe pump, gas cylinder, and gas lines. The gas lines were plastic tubes. Two solenoid valves (Asco Red-Hat 8262H202 for Solenoid valve-1, Parker Hannifin 009-0272-900 for Solenoid valve-2) remotely opened and closed the gas line. In between the two solenoid valves, a digital flowmeter (Aalborg, XFM17) was installed for flow rate measurement via a RS232-1 interface for the constant flow bubble case. The flow rate for a few bubble case was controlled by the syringe pump with a pre-determined value. The gas under test was injected into the water column through a syringe needle. A check valve was used to prevent water from entering back into the needle. The syringe needle was replaceable with a variety of needle apertures. PVC pipes (6" in diameter) were used to construct a bubble generation enclosure to contain the bubble generation system and allow it to be submerged in the water tank. Several lead bricks were placed inside the enclosure to counteract the buoyancy force.

The second bubble source was a simple bubble generation apparatus that consisted of a needle, a check valve, an aluminum cylinder to anchor the bubble source on the floor of the water tank. A long plastic tube connected between the needle and a syringe that was used to manually push gases under test out of the needle. There is no flowrate control and measurement for this apparatus. This bubble source was employed only for localization purpose and was able to change its position around the tank.

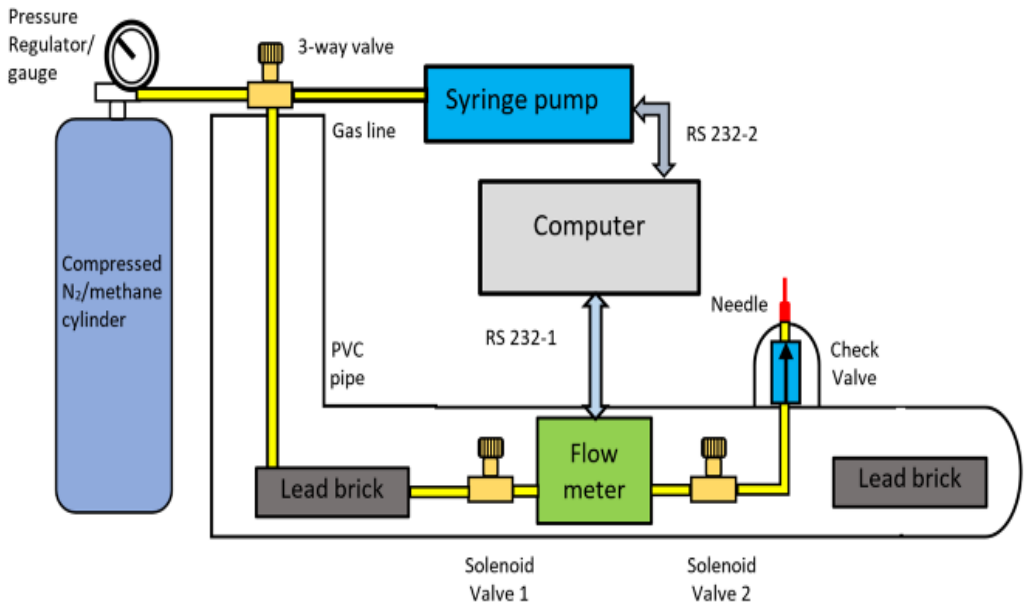

Fig. 3.1. The schematic diagram of the bubble generation system.

Figure 3.2 shows a top-view and a 3D view of the placements of two active hydrophone sources (S1 and S2), and two bubble sources (S3 and S4), a passive hydrophone network (CH1-CH7), and five passive linear hydrophone arrays (V-A1-V-A3; H-A4 and H-A5), respectively.

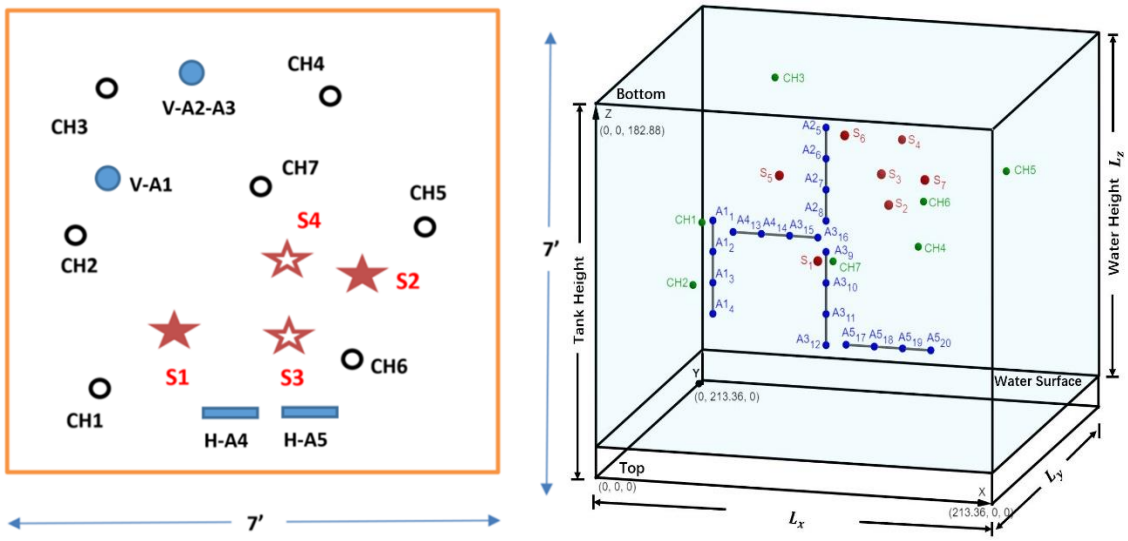

Fig. 3.2 (a) The top view and (b) 3D view of acoustic sources (S1- S4), hydrophones (CH1-CH7), and vertical and horizontal hydrophone arrays (V-A1, V-A2, V-A3, H-A4, and H-A5)

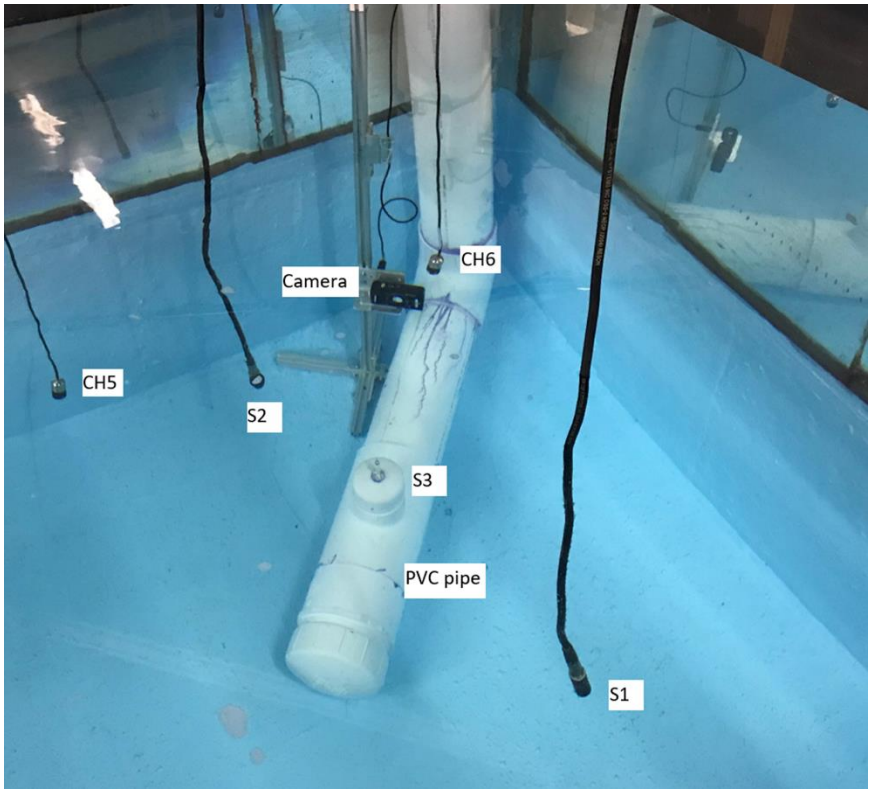

Fig. 3.3 the photo of the experimental setup

Figure 3.3 is a photo that shows parts of the experimental setup, where two active hydrophone sources S1 and S2, the bubble source S3, two passive hydrophones CH5 and CH6, the bubble generation enclosure PVC pipe, and the underwater camera are visible.

Two omnidirectional hydrophones (Teledyne RESON, TC4040) S1 and S2 were served as active hydrophone sources. The active hydrophones can emit underwater sounds when excited by amplified electrical signals from a function generator or from a data acquisition board. With their controllable signal sources and known coordinates they were used for testing and verifying localization algorithms. They can also alternatively be used as noise sources during bubble source localization.

Figures 3.4-3.5 illustrate the schematic diagrams of the instrument control and data acquisition system.

In Figs. 3.4-3.5, a function generator (Agilent 33120A) generated predefined tone-burst, pulse, step function signals, and noise, respectively. In addition, a chirp signal was created by a data acquisition board (NI USB-6349) via an analog output (AO) in Fig. 3.5. These electrical signals were amplified by a power amplifier (Krohn-Hite Model 7500 amplifier) and fed to one of the active hydrophones. A synchronized signal from the function generator was used as Trigger 1 to synchronize the data acquisition. For the chirp signal, the trigger signal was generated and detected inside the data acquisition board.

In Fig. 3.4, seven passive omnidirectional hydrophones (Aquarian, H1a) from CH1 to CH7 were randomly distributed around the sources (S1-S4) in the water tank to form a hydrophone network. These hydrophones were amplified by pre-amplifiers (Stanford Research System, Inc. SR650) and the signals were fed to the

input channels of two oscilloscopes (Agilent, infinium) and transferred to the computer via two IEEE 488 interfaces (GPIB1 and GPIB2). A bubble signal from one of the hydrophones (CH4 or CH7) was used as Trigger 2 to synchronize the data acquisition. A home-made electronic circuit (not shown in Figs. 3.4-3.5) using a Schmitt-trigger inverter IC (74HC4N, Texas Instruments) converted the analog signal from the hydrophone into a TTL signal as Trigger 2.

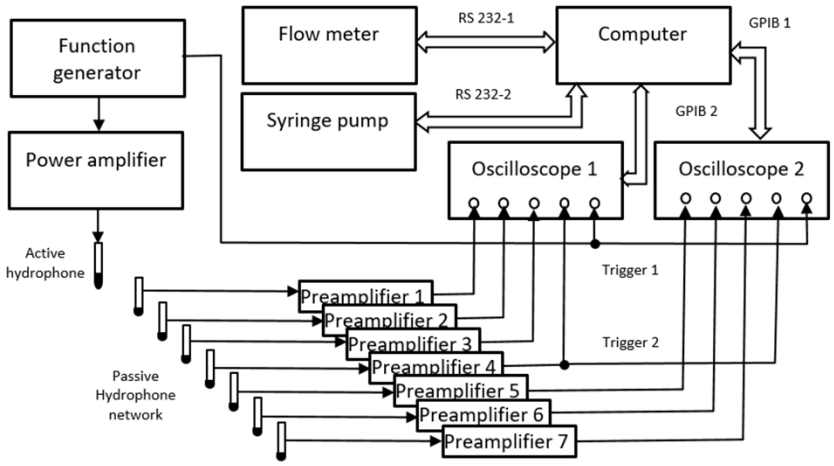

Fig. 3.4 The schematic diagram of the instrument control and data acquisition for hydrophone network

In order to localize bubble sources using direction of arrival (DOA) algorithms, five linear hydrophone arrays (V-A1, V-A2, V-A3, H-A4, and H-A5) were employed in the water tank (Fig. 3.2). Each hydrophone array consisted of four passive omnidirectional hydrophones (Aquarian, H1a) with an equal spacing of 15.2 cm. Among them, V-A1, V-A2 and V-A3 were vertical hydrophones arrays and H-A4 and H-A5 were positioned horizontally parallel to the water surface. In this testing configuration, all hydrophones including hydrophone network and arrays were amplified by hydrophone preamplifiers (Aquarian Scientific, PA4-DC) and the amplified signals were acquired by a data acquisition board (NI USB-6349) that simultaneously sampled total twenty-seven hydrophone (CH1-CH7; five arrays) signals at maximum sampling rate of 400 kHz. The trigger signals were the same as those described previously. The acquired signals were transfer to the computer via RS 232-3 interface.

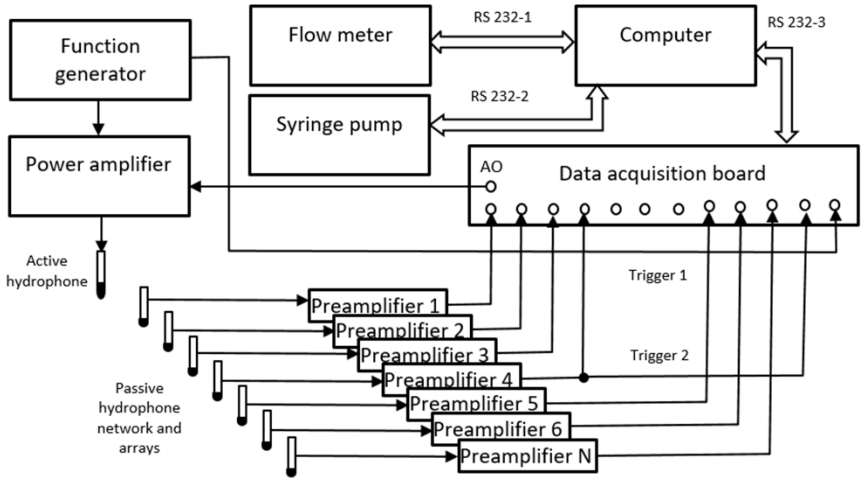

Fig. 3.5 The schematic diagram of the instrument control and data acquisition for both hydrophone network and hydrophone arrays

The whole measurement system was automated with a program written in LabView for instrument control/measurement, active source generation, data acquisition, signal processing, and data analysis.

A digital underwater camera (TG-5, Olympus), as shown in Fig. 3.3, recorded movies that captured the processes of bubble movements at 240 frame/s. Fig. 3.6(a) shows an example for a few bubbles case where two bubbles occur and Fig. 3.6(b) presents a typical photo of the constant flow bubble case where cloudy bubbles with different sizes appear. The corresponding movie data for the two cases can be found in the data repository website of the UM eGROVE (https://egrove.olemiss.edu/grpds).

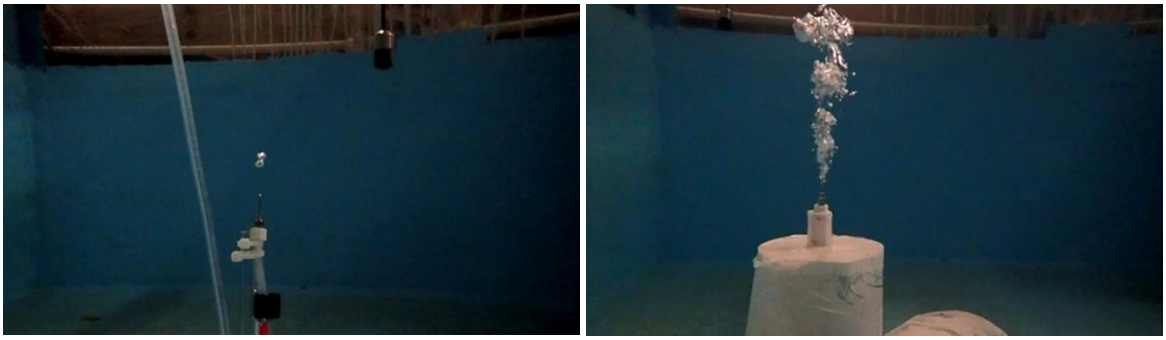

Fig. 3.6 (a) the photo of a few bubble case, (b) the photo of the constant flow bubble case.

3.2 Experimental results

3.2.1 A few bubble cases

In a few bubble case, two motivations served for the study. One was to simulate seafloor seepage and the other was to establish the correlation between the resonant frequency and crack size. For the former, the syringe pump was programmed to create gas flows at very low flow rates ranging from 5μL/min to 200μL/min, attempting to generate a single bubble in a quasi-static manner. However, it was found that even at the lowest flow rate of 5μL/min, it was very difficult to generate a single bubble. In most cases, a few (two or three) bubbles emerged from the needle almost concurrently, as seen in Fig. 3.6(a). For the latter motivation, a number of syringe needles with standard gauge numbers from G12 to G24 were employed. These needles have a blunt tip. Table 3.1 listed the diameter of needles with different gauge number.

Table 3.1 The diameters of syringe needles with different gauge number

Gauge number	G12	G14	G16	G18	G20	G21	G22	G24
Diameter (mm)	2.16	1.6	1.19	0.84	0.6	0.51	0.41	0.31

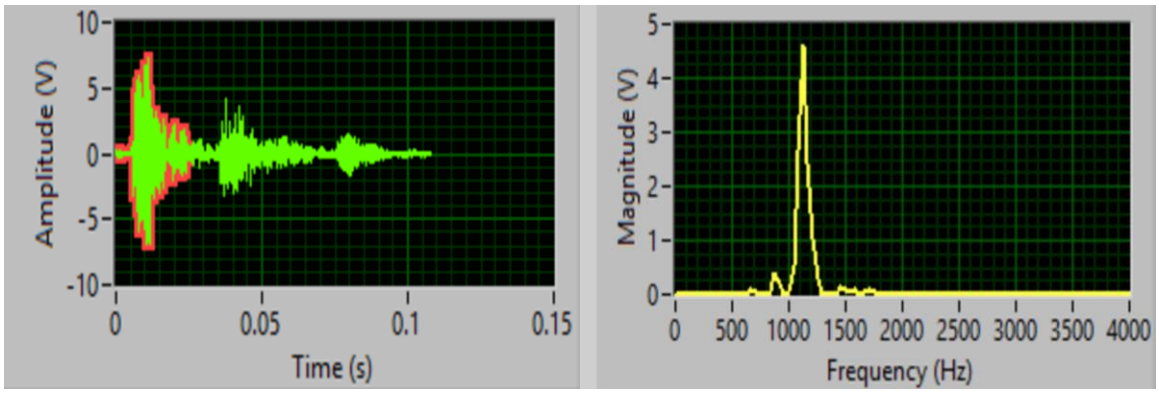

Fig. 3.7 acoustic signals in time and frequency domains for a few bubble case. In Fig. 3.7(a), the first predominant time trace was selected by a time window for determining the resonant frequency.

Figure 3.7 shows a typical acoustic signal in both time and frequency domains for a few bubble case. The time trace in Fig. 3.7(a) consisted of the direct bubble sound and a series of echoes (signals reflected from the boundaries of the water tank). The resonant frequency of an individual bubble event was obtained by selecting the first predominant time-trace of the bubble sound using a time window as shown in Fig. 3.7(a) and performing a fast Fourier transform FFT as shown in Fig. 3.7(b). It was found that each bubble event often yielded slightly different frequency responses. Video recordings (like Fig. 3.6(a)) revealed that the bubbles in the subsequent events featured slightly different shape deformations (non-spherical bubbles) and sizes even at the same flow rate. These inconsistencies among bubble events contribute to the variations of the resonant frequency. For this reason a statistic method was used to determine the resonant frequency. For a specific needle and a fixed flow rate, tens of bubble events were recorded and their resonant frequencies were measured and compiled in histograms as shown in Figs. 3.8-3.10, where the y-axis is the count of bubble events and x-axis is the resonate frequency, and the peak of the histogram was determined as the resonant frequency.

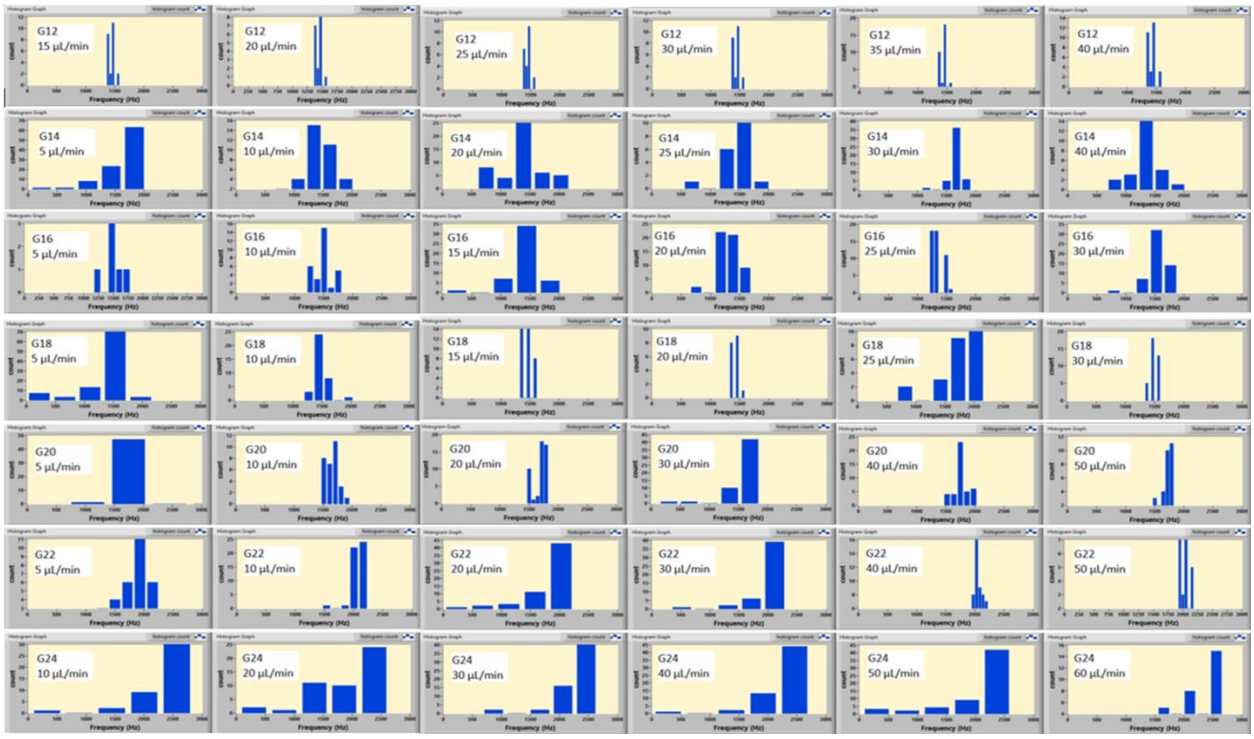

Fig. 3.8 Histograms of the resonant frequency for nitrogen-1

The a few bubble test for nitrogen was conducted twice with slightly adjusted flowrates and the results are shown in Figs. 3.8-3.9.

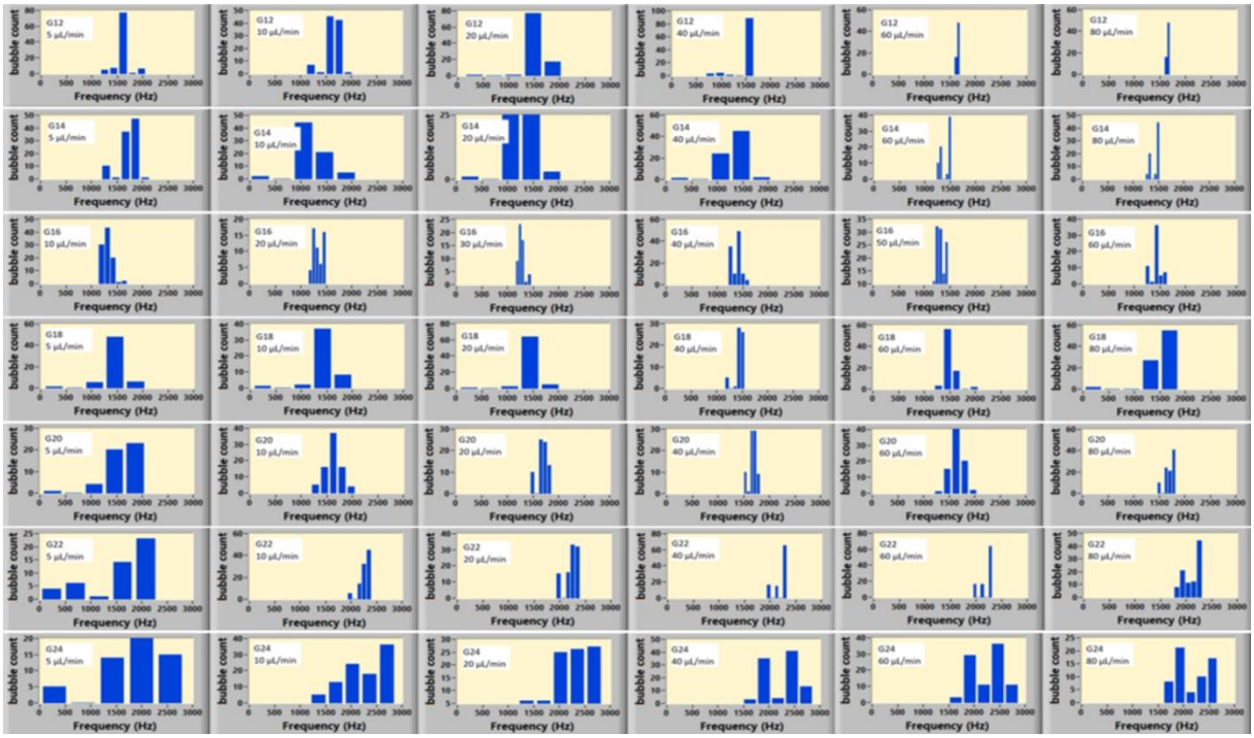

Fig. 3.9 Histograms of the resonant frequency for nitrogen-2

In the above a few bubble tests for nitrogen, the minimum flow rate was 5 µL/min. At this flow rate, it took very long time to generate one bubble event. In order to speed up the bubble occurrence rate, for a few bubble tests of methane, the flow rate range was set to be from 20 µL/min to 200 µL/min. The resonant frequency histograms of methane for different needles and flow rates were displayed in Fig. 3.10.

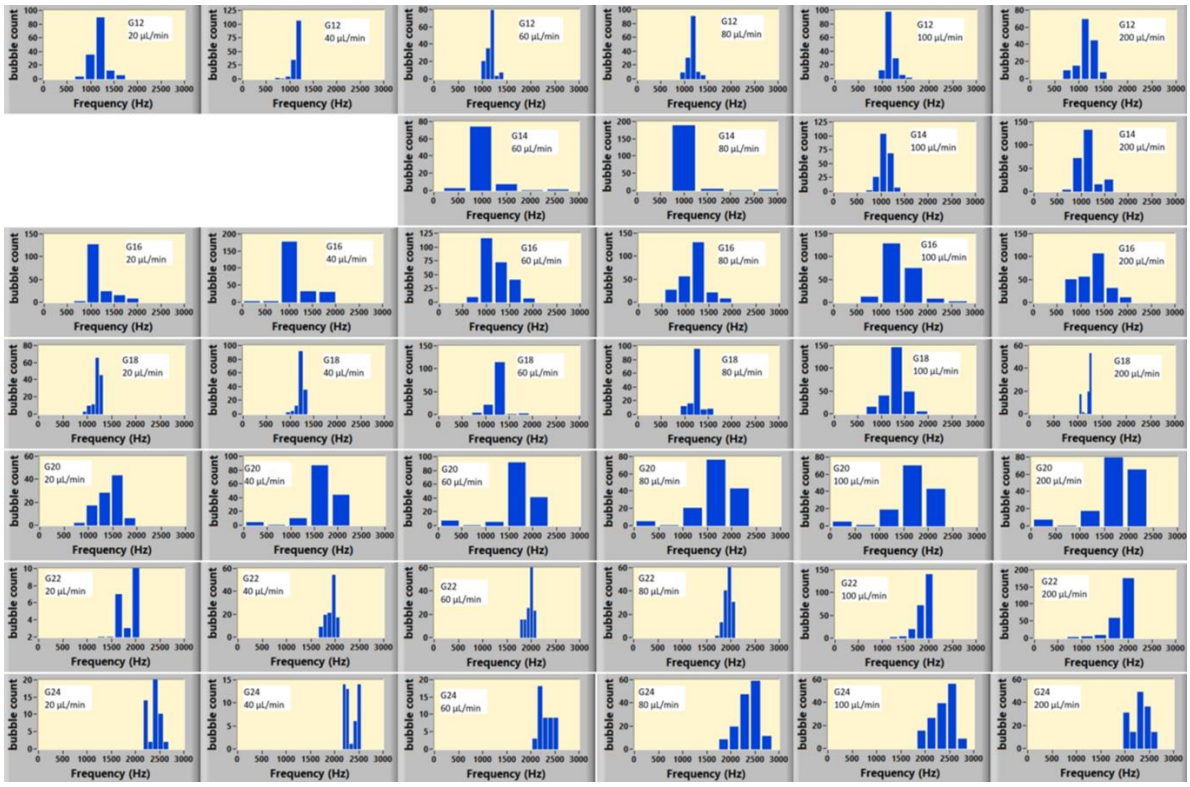

Fig. 3.10 Histograms of the resonant frequency of methane

The above obtained resonant frequencies from the histograms of both nitrogen and methane vs needle diameter along with the different flow rates are displayed in Fig. 3.11, where µL/min in the legend denotes the flow rate. When one examines the data for a specific needle with different flow rates, the resonant frequencies are relatively scattered, as presented as vertical lines in Fig. 3.11 for a certain needle diameter. No common trend can be found between the resonant frequency and flow rate. As mentioned before, the bubbles were generated in a quasi-static manner at very low flow rates. Each bubble event occurred intermittently. The changes of these flow rates affected only the time intervals of bubble occurrence and have negligible effects on bubble behaviors of both physical and acoustic properties.

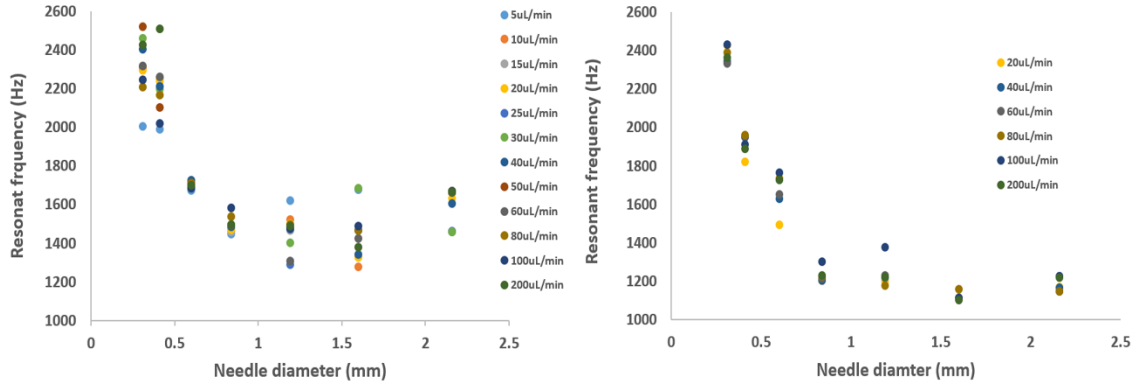

Fig. 3.11 the resonant frequency vs the needle diameter for (a) nitrogen and (b) methane

In general, the resonant frequency decreases with the increment of the needle diameter. More detailed analysis will be presented in acoustic modeling section.

3.2.2 The constant flow bubble cases

For the constant flow bubble case, the gas under test was injected into the water at a constant flow rate. As seen in Fig. 3.2(b), the injected gas formed a cloud of bubbles with different bubble sizes which created a broadband signal with frequencies ranging from 300 Hz to 2500 Hz, as shown in Fig. 3.12.

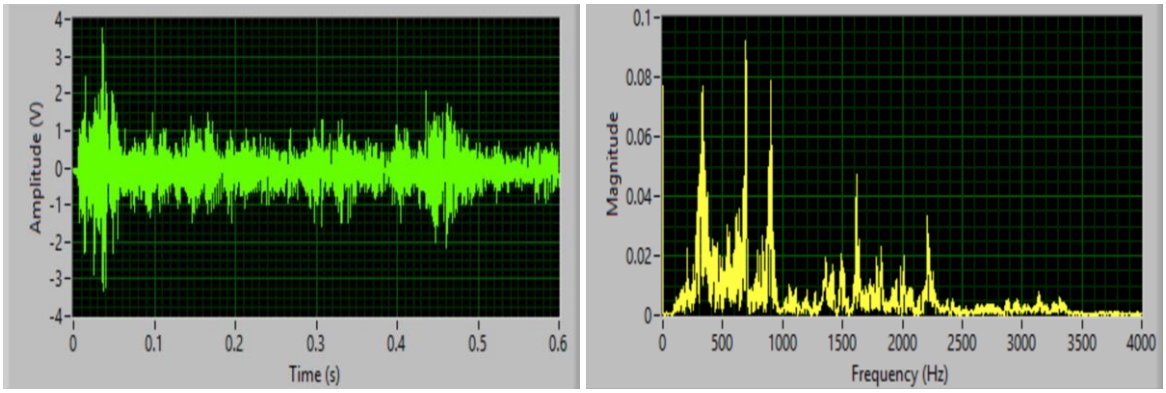

Fig. 3.12 acoustic signal in time and frequency domains for the constant flow rate case.

This broadband signal features several distinctive frequency peaks that could be utilized to estimate the bubble size distributions [Leighton and Walton, 1987], which will be described in the acoustic modeling section. In this section, we focused our attention on the total energy and its relationship with flow rate and jet velocity. The total energy was defined as the summation of the squared frequency magnitude spectra over a certain frequency range, say from 300 Hz to 2500 Hz. The duration of the time signal for performing the FFT was 0.3 s. The jet velocity was calculated by dividing the flow rate with the interior area of a needle.

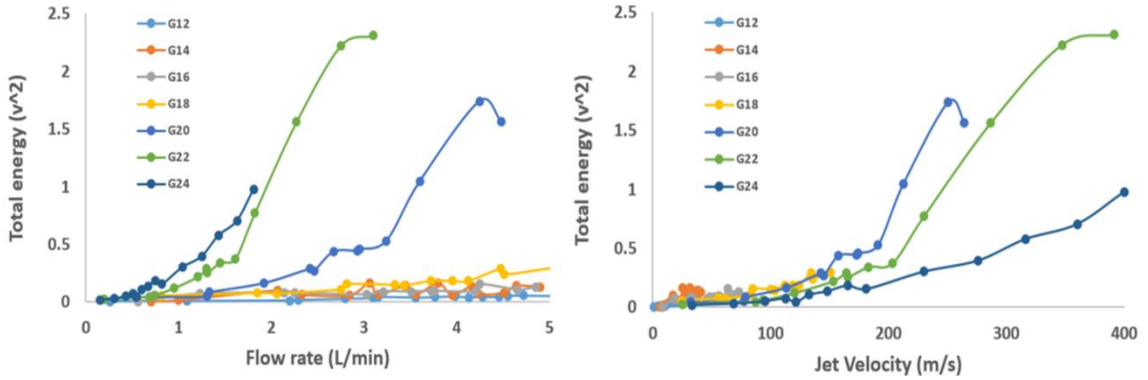

Fig. 3.13 (a) Total energy vs flow rate and (b) total energy vs jet velocity of nitrogen

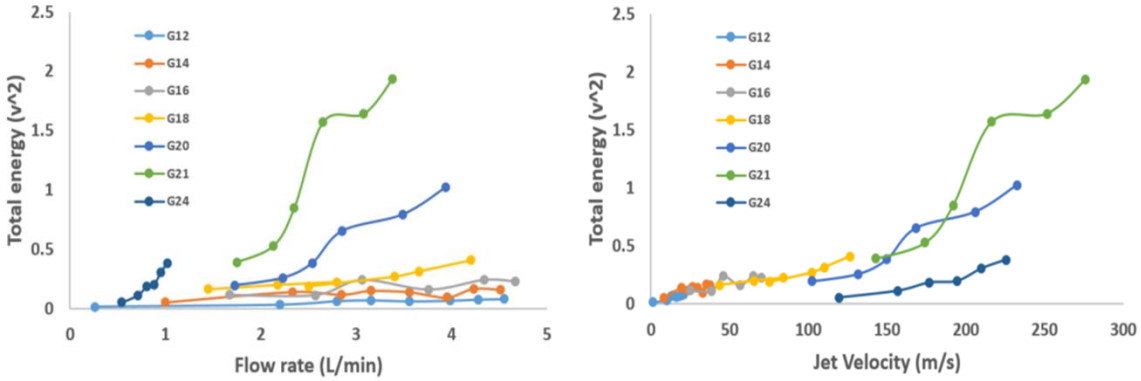

Fig. 3.14 (a) Total energy vs flow rate and (b) total energy vs jet velocity of methane

Figs. 3.13(a)-3.14(a) show the total energy vs flow rate and Figs. 3.13(b)-3.14(b) display the total energy vs jet velocity for both nitrogen and methane with different needle gauge numbers, respectively. Note that for nitrogen the syringe needle with G22 was tested whereas for methane the G21 syringe needle was used. As seen in Figs. 3.13-3.14, the total energy increases with both the flow rate and jet velocity. The trends of the total energy vs flow rate are spread widely among the different needles, whereas the total energy vs jet velocity curves seem closer to each other, implying that the jet velocity is a governing factor that controls the total energy. Further discussions will be addressed in the following section of acoustic bubble modeling.

3.2.3 The shearing and turbulence sound study

In our proposal, it was initially speculated that there was a second oil-spill related underwater sound mechanism: streaming jet through shearing and turbulence effects. To study this hypothesis, a peristatic pump (JIH-Pump, 253Yx, Chonqing Jieheng Peristaltic Pumps CO., LTD) was employed to create water streaming jet with pre-defined flow rates using tap water. The syringe needles with different needle diameters were tested. In conducting the experiments, precaution was taken to generate only pure water jets without introducing bubbles. It was found that no significant sound was detected within the testing flow rate range for all needle tested. It is therefore concluded that the underwater sound created by steaming jet through the shearing and turbulence of pure liquid (tap water, in this study) is negligible as compared with the sound created by bubble oscillations.

3.2.4 Conclusion and summary for the experiments

The acoustic behaviors of bubbles caused by oil leakages were studied in a laboratory under controlled conditions such as flow rate, types of oil leakages, crack sizes, and gases. Specifically, two types of oil leakages were simulated: a few bubble case for oil seepage from sea-floor and the constant flow case for the situation of broken wellheads or pipelines. For a few bubble case, the resonant frequency decreases with the increment of the needle diameter. For the constant flow rate cases, the total energy increases with both the flow rate and jet velocity. It is found that the underwater sound created by steaming jet through the shearing and turbulence of pure liquid (tap water, in this study) is negligible as compared with the sound created by bubble oscillations.

4. Acoustic Bubble Modeling

For **Task 2,** we implement the theory of bubble dynamics to understand the data taken from the water tank experiments as described above. In particular, we consider (1) the dependence of the resonant frequency on the size of crack, (2) the dependence of the sound intensity in terms of the total energy on the oil leak flow rate and jet velocity, and (3) the bubble size distribution. The understanding aims to guide the assessment of the features of oil leakage from the recorded sound signals.

4.1 The dependence of the resonant frequency on the size of crack

In the cases of a few bubbles, the relation between the resonant frequency and the needle diameter, which mimics the crack size of the oil leakage, was established. Since no significant difference between nitrogen and methane was found at present testing conditions, the data of the resonant frequencies for both nitrogen and methane are put together and plotted in Fig. 4.1(a).

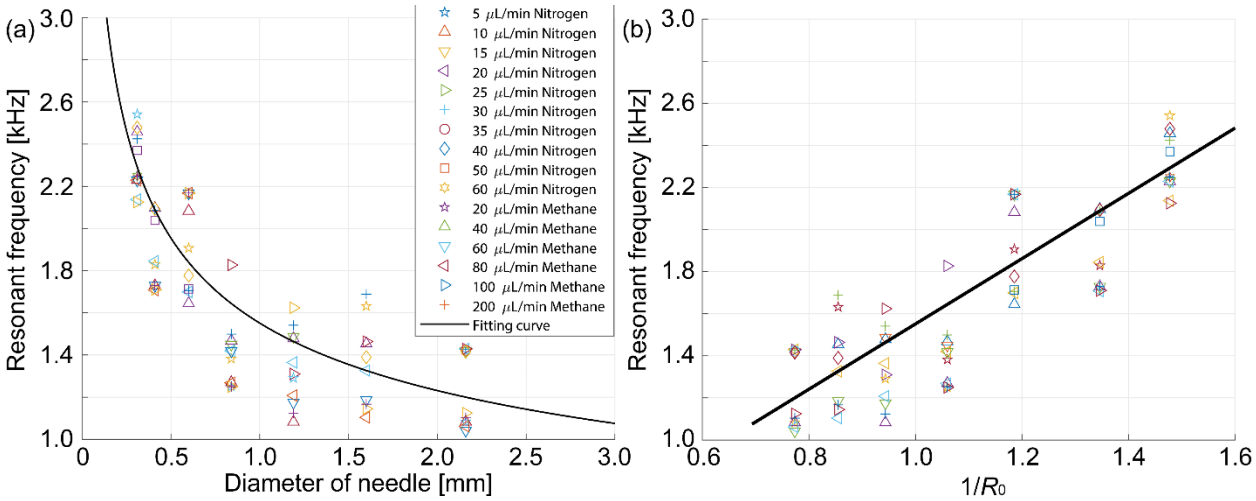

Fig. 4.1(a) The resonant frequency vs the diameter of the needles, where μL/min in the legend denotes the flow rate and the solid line is the regression line, and (b) The resonant frequency vs $1/R_0$, where R_0 is the effective radius of a spherical bubble.

The overall data in Fig. 4.1(a) reveals a nonlinear decreasing trend in the resonant frequency as the needle diameter increases. This trend can be curve-fitted into a solid line in Fig. 4.1(a) as a regression curve, expressed by:

$$f = AD^{-1/3}, \tag{4.1}$$

where f is the resonant frequency, D is the diameter of needles, A is a constant, which yielded a coefficient of correlation $|r|^2$ of 0.8 and an A value of 1551.

From bubble dynamics point of view, when the bubble reaches its maximum volume, it starts to detach from the needle. Needles with different diameters have different maximum bubble volumes, which correspond to different acoustic frequencies. According to the analysis of bubble dynamics (Longuet-Higgins, et al, 1991), the resonant frequency is proportional to the needle diameter to the power minus one third [f~D^(-1/3)]. Our experimental results are in good agreement with this theoretical model. Furthermore, according their study, a single spherical bubble volume is proportional to the needle diameter. As such, the Eq. (4.1) can be reduced into a formulae expressed by:

$$f=A'/R_0, \tag{4.2}$$

where A' is an adjustable constant and R_0 is the effective bubble radius. This new equation is in the form of the well-known Minnaert [1933] resonant frequency for a pulsating spherical bubble. To demonstrate this relationship, the resonant frequency *vs* $1/R_0$, is plotted in Fig. 4.1(b), where R_0 is the radius of a spherical bubble and the solid line is a linear regression with a coefficient of correlation of $|r|^2$ of 0.8.

The observation as presented in Eq. (4.1) could be useful in estimating a crack size from the recorded oil spill-induced sounds, which indicated that the higher the frequency of bubble sound, the smaller the size of a crack.

4.2 The dependence of the total energy on the flow rate and jet velocity

In the constant flow bubble cases, we also put the data of the total energy for both nitrogen and methane together, as shown in Figs. 4.2(a)-4.2(b).

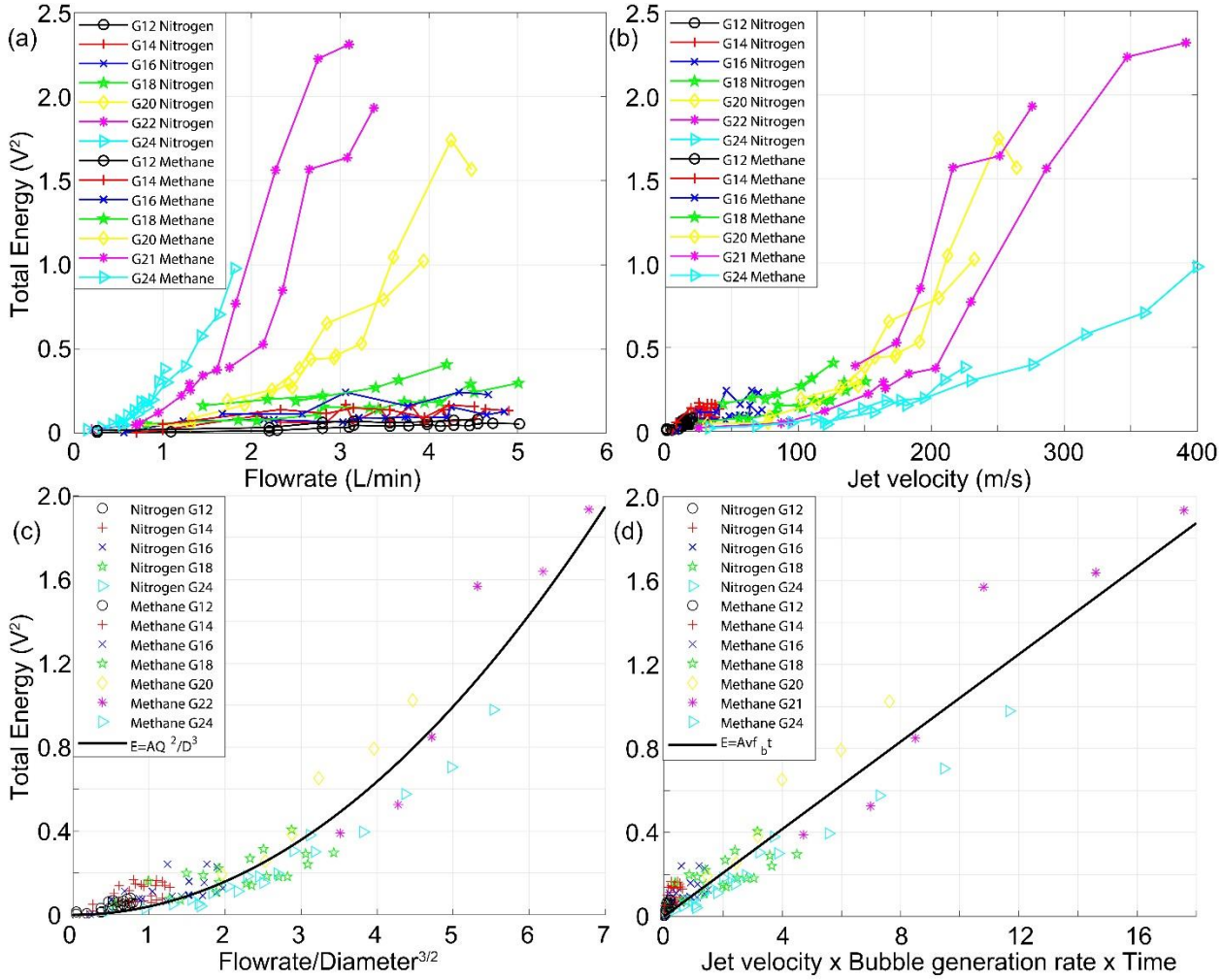

Fig. 4.2(a) Total energy vs flow rate, (b) total energy vs jet velocity, (c) total energy *vs* flowrate^3/diameter^2, and (d) total energy vs jet velocity× bubble generation rate×time.

After data analysis, an empirical relationship was found among the total energy, flow rate, and needle diameter, expressed by

$$E=BQ^2/D^3t \tag{4.3}$$

where E denotes the total energy, Q is the flow rate, B is a constant, and t is the time duration of the signal (t=0.3 s, in the study) (see Fig. 4.2 (c)).

To better understand this correlation, we assumed that the total energy is a summation of the energy carried by each individual bubble. We further approximated that each single bubble features an identical effective volume. As mentioned before, this effective single bubble volume is proportional to the needle diameter. Using these approximations, we can rewrite the above Eq. (4.3) in the form expressed as

$$E=Cvf_bt \tag{4.4}$$

where v is the jet velocity that is proportion to Q/D^2, and f_b is the bubble generation rate that is defined as the flow rate divided by the effective single bubble volume and is proportional to Q/D. As seen in Fig. 4.2(d), this equation formed a solid line that fitted all experimental data quite well with a coefficient of correlation $|r|^2$ of 0.9. In Eq. (4.4), the term Cv is interpreted as the energy carried by an effective single bubble and the term f_bt represents the total bubble number.

Generally speaking, higher jet velocity can cause higher deformations of bubbles deviating from pure spheres. These distorted bubbles exhibit more oscillation modes than a monopole mode and thus produce greater acoustic energies. Therefore the energy carried by an effective single bubble is proportional to the jet velocity. On the other hand, as the bubble generation rate f_b increases with the flow rate for a certain needle, more bubbles are created and the chance for bubble coalescence increases. A study [Manasseh *et al*., 2008] demonstrated that the sound created by bubble coalescence has an order of magnitude greater amplitude than the sound created by a bubble pinched off from the needle. These two effects contribute to the total energy for the constant flow case.

The developed acoustic bubble modeling enhanced our understanding of the underlying mechanisms of bubble-induced sounds.

4.3 The bubble size distribution

For the constant flow bubble case, the injected gas formed a cloud of bubbles with different bubble sizes which created a broadband signal with frequencies ranging from 300 Hz to 2500 Hz, as shown in Fig. 3.12. This broadband signal features several distinctive frequency peaks that could be utilized to estimate the bubble size distributions (Leighton and Walton, 1987). Typical frequency spectra under several pressure conditions for nitrogen gas with the needle G14 were shown in Fig. 4.3(a). Specifically, Fig. 4.3(b) shows the frequency spectrum under pressure of 10 psi with the peak frequencies marked. These peak frequencies were used to calculate the corresponding bubble sizes (also marked in the Fig. 4.3(b)). The bubble radius was calculated from the frequency spectrum by using the well-known Minnaert resonant frequency formula (Minnaert, 1933), expressed by,

$$f = \frac{1}{2\pi a}\sqrt{\frac{3\gamma P}{\rho}} \tag{4.5}$$

where f is the frequency, a is the radius of the bubble, γ is the specific heat ratio of the gas, P is the hydrostatic pressure, ρ is the density of the liquid. Let us take Nitrogen gas and G14 needle as an example, which gives γ=1.404 at temperature of 300 K, P = 101 kPa, ρ =*1000* kg/m^3.

The distinctive frequency peaks in Fig. 4.3(b) reveal the discrete nature of the bubble size distribution from about 1 mm to 5 mm. Inset in Fig. 4.3(b): corresponding photo with some referenced bubble sizes were marked. It is generally believed that for constant flow case, the low frequency portion of the sound signal mainly comes from the coalesced bubbles with relatively large radius. However, the high frequency of the bubble sound almost directly generated by small bubbles released from the needles.

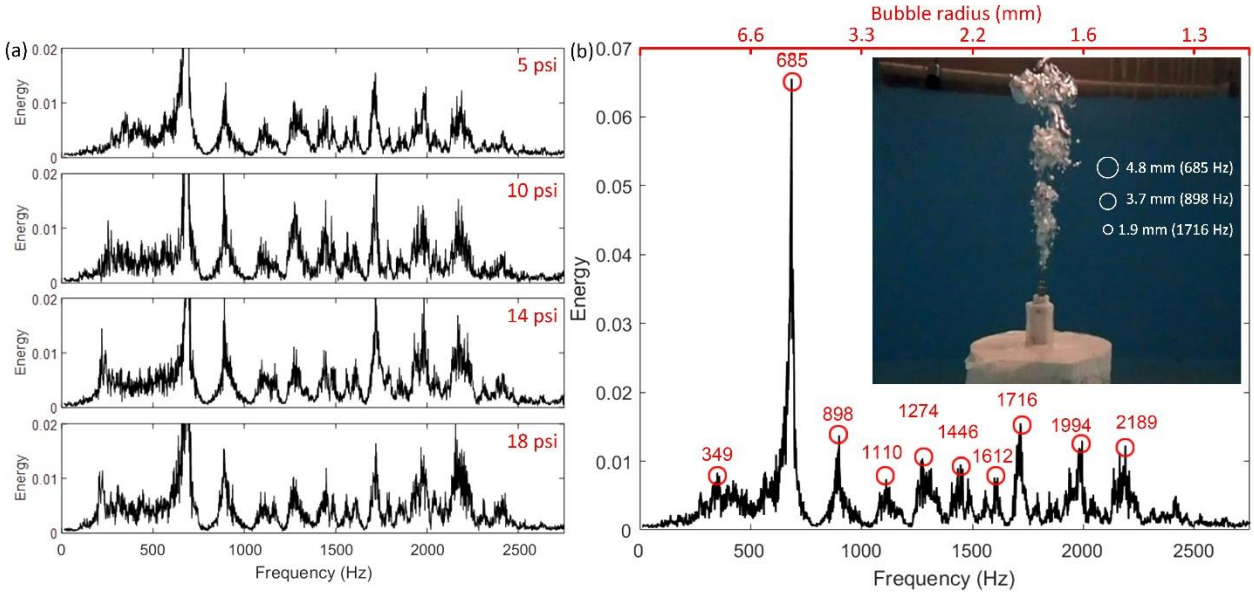

Fig. 4.3(a) Sound frequency spectrum for several pressure for nitrogen gas with the needle number being G14. (b) Frequency spectrum under pressure of 10 psi with the peak frequencies and corresponding bubble distribution marked. Inset: corresponding photo with some referenced bubble size marked.

We further normalize the frequency spectrum as shown in Fig. 4.3. In general, we find that for a specific needle, the higher the pressure, the more proportion of relatively smaller radii bubbles are generated. The reason is that for high pressure condition, the bubbles are much easier to break due to the high jet velocity. Similar phenomena are also observed in other needles and for Methane gas (results are not presented here).

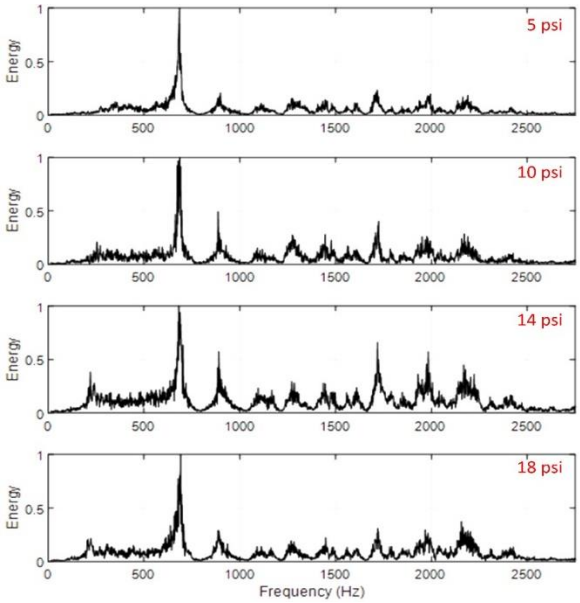

Fig.4.4 (a) Sound frequency spectrum normalized by respective maximum value in Fig. 4.3(a) for different pressure conditions for G14 needle.

We further examine the normalized frequency spectrum (averaging over all pressure conditions for a specific needle) for different needles with Nitrogen gas as shown in Fig. 4.5(a). This normalized spectrum can exhibit the overall characteristics from a specific needle for the dependence of bubble size distribution on the needle diameter, where the small bubble radii correspond to the high frequencies and large bubble radii correspond to the low frequencies. We find that for different needles, the smaller the needle diameter, the more proportion of relatively smaller radii bubbles are generated, which is consistent with the results in single bubble generation. Similar results are also found for Methane gas as shown in Fig. 4.5(b).

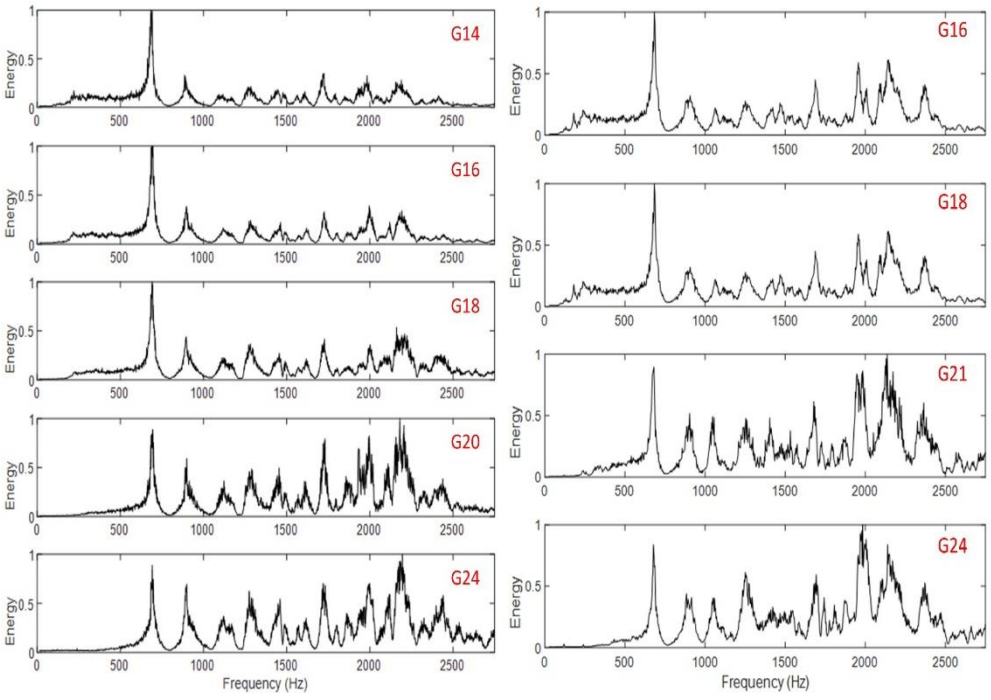

Fig. 4.5 Normalized sound frequency spectrum for different needles for (a) Nitrogen gas and (b) Methane gas.

In order to obtain the bubble size distribution, the acoustic power emitted from a single bubble needs to be examined. The sound pressure generated by a single bubble with a radius *a* can be expressed as follows, (Leighton and A. Walton, 1987)

$$p = \frac{3A_0\gamma P}{[a^2+\frac{3\gamma P r^2}{\rho\ c^2}]^{1/2}}, \tag{4.6}$$

which assumes a simple harmonic motion of the bubble surface with A_0=10^{-8} being the initial vibration amplitude of the bubble , c = 1500 m/s being sound speed of the fluid, $r = 1.15$ m being the distance between the needle and the hydrophone.

Figure 4.6 shows a weighting function E_0 ($E_0 = p^2$) versus bubble radius, which represents the variation of acoustic power as a function of single bubble radius. The result shows that the radiated power of the bubble source decreases with the bubble radius. (Note: In this case, the value of $\frac{3\gamma P}{\rho}\frac{r^2}{c^2}$ is ~2.5e-4 and for the bubble radius range considered here, i.e. 1 mm to 10 mm, the ratio of $a^2/\frac{3\gamma P}{\rho}\frac{r^2}{c^2}$ is within the range of 4% to 40%.)

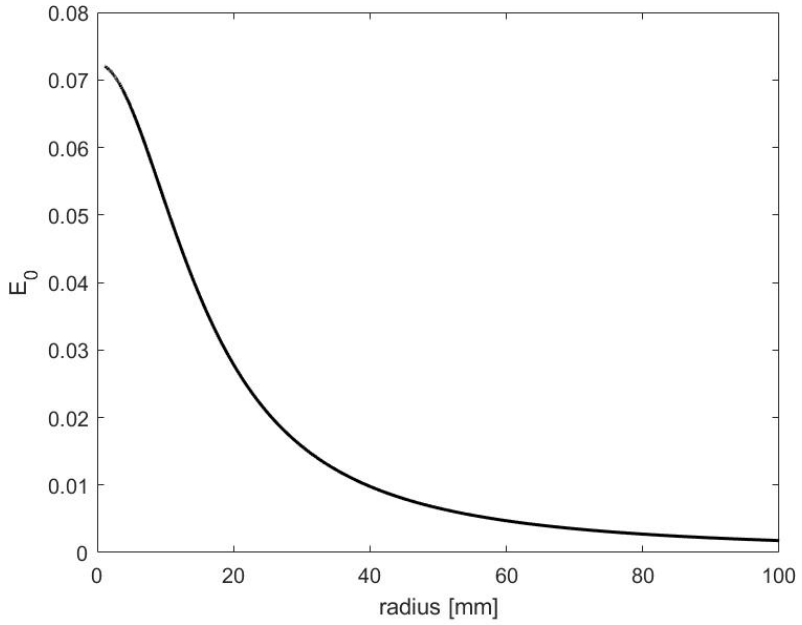

Fig. 4.6 Weighting function E_0 as function of bubble radius.

The number of bubbles for specific radius can be obtained by the power spectrum in the bubble radius domain divided by the weighting function with the normalization determined by the total volume of the Nitrogen gas injected into water (Fig. 4.7).

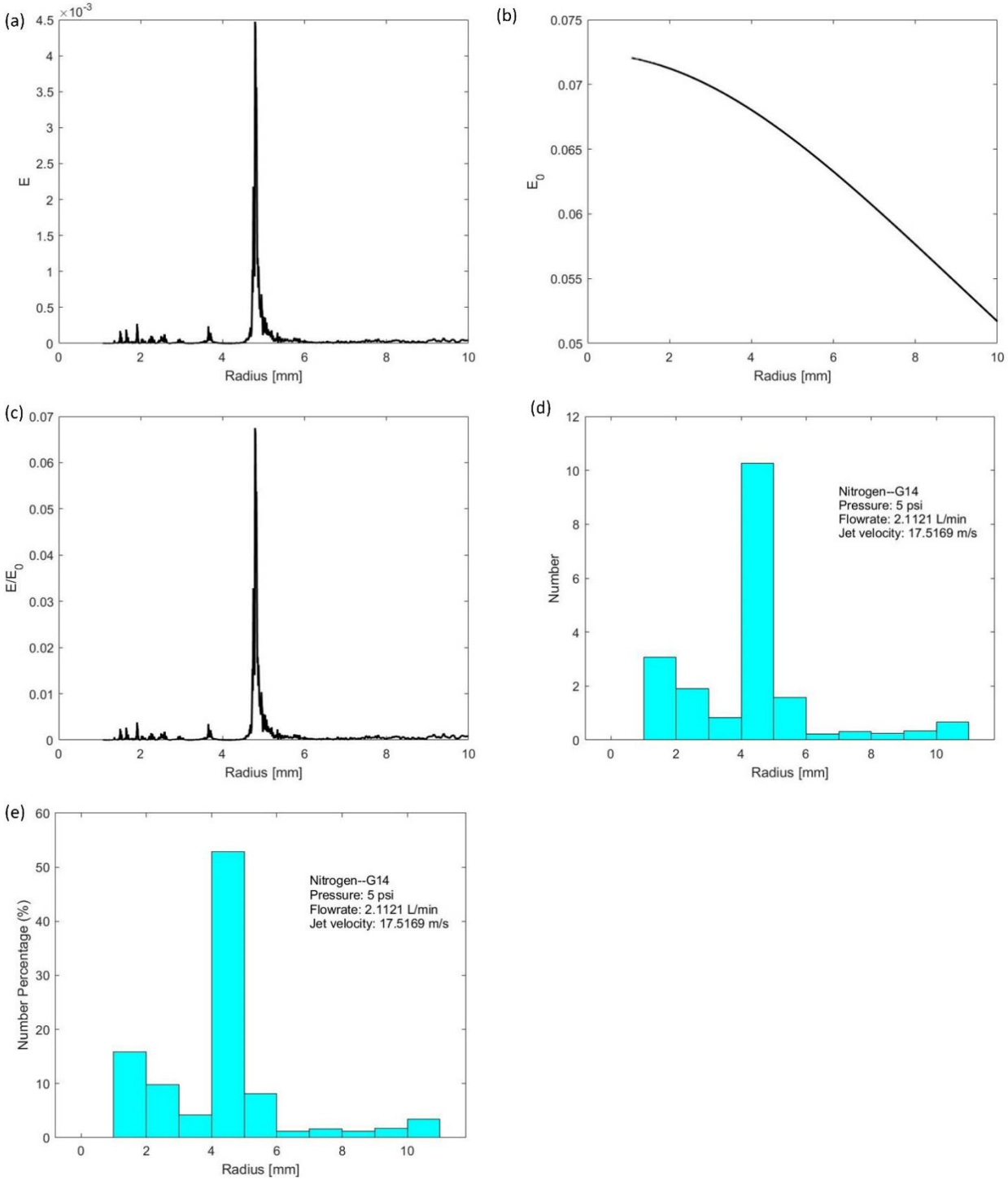

Fig. 4.7 Procedure to compute bubble population histogram (a) converted bubble radius domain, (b) the weighting function, (c) the effective bubble number, and (d) bubble number distribution, (e) bubble number percentage distribution

One can write the procedure out explicitly:

(1) Converting the power spectrum in the frequency domain into the radius using the well-known Minnaert resonant frequency formula (Minnaert, 1933), see Fig. 4.7(a);
(2) Dividing the power from each bubble radius by the weighting function [Fig. 4.7(b)] element-wisely to obtain the effective bubble number ($N_{eff} = E/E_0$) in Fig. 4.7(c);
(3) Integrating the effective bubble number on the bubble volume to obtain the effective total bubble volume V_{eff}, which should be equal to the gas volume ($V=Qt$) except a pre-factor A, i.e. $AV_{eff} = V$.
(4) The bubble number N can be obtained by the pre-factor A times the effective bubble number N_{eff}, i.e. $N = AN_{eff}$, see Fig. 4.7(d)
(5) Using the bubble number from each radius divided by the total bubble number (obtained by the summation of all the bubble number over all the range of the bubble radii) to obtain the bubble number percentage; see Fig. 4.7(e).

Bubble population histogram for Nitrogen gas with G14 needle for different pressure conditions are shown in Fig. 4.8 as a demonstration. Two dominant peaks for all pressure conditions appear around the ranges of 1-2 mm and 4-5 mm with the total number percentage of these two ranges larger than 60%.

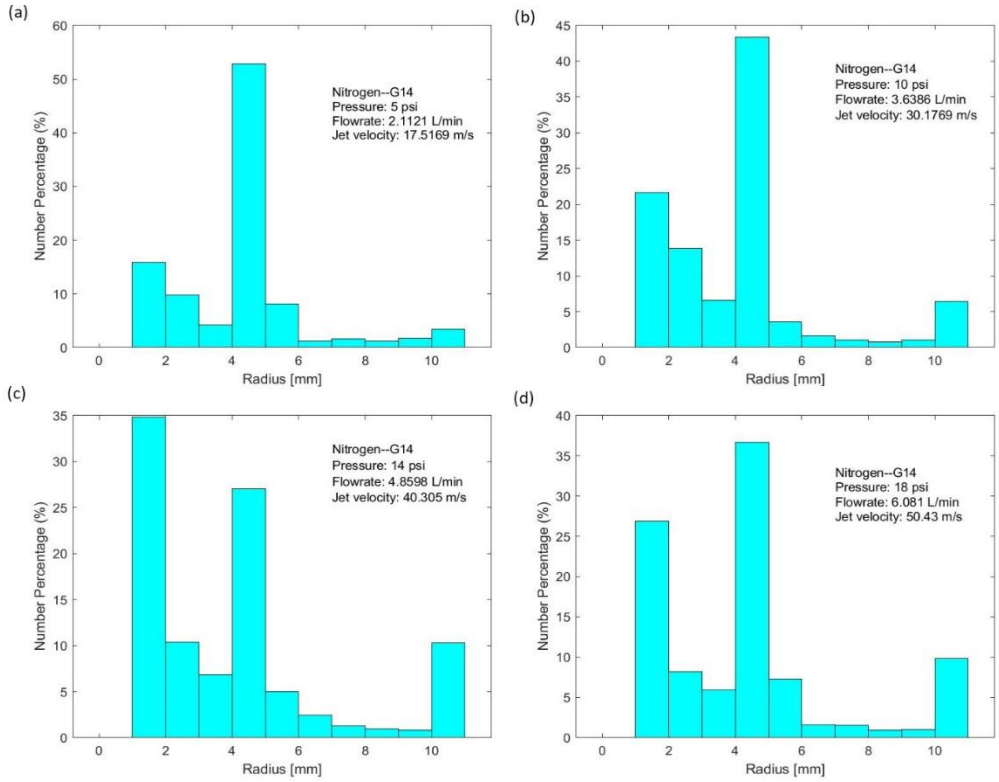

Fig. 4.8 Bubble number percentage histogram for Nitrogen gas with G14 needle.

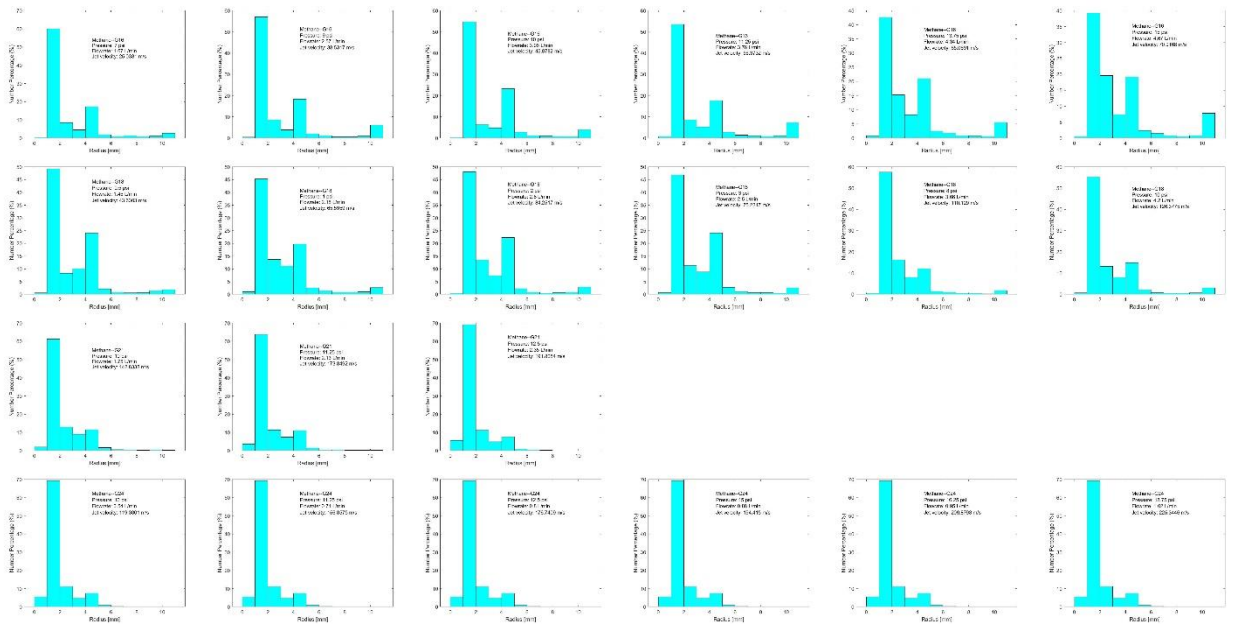

Fig. 4.9 Bubble number percentage histogram for methane gas with all needles and flowrates.

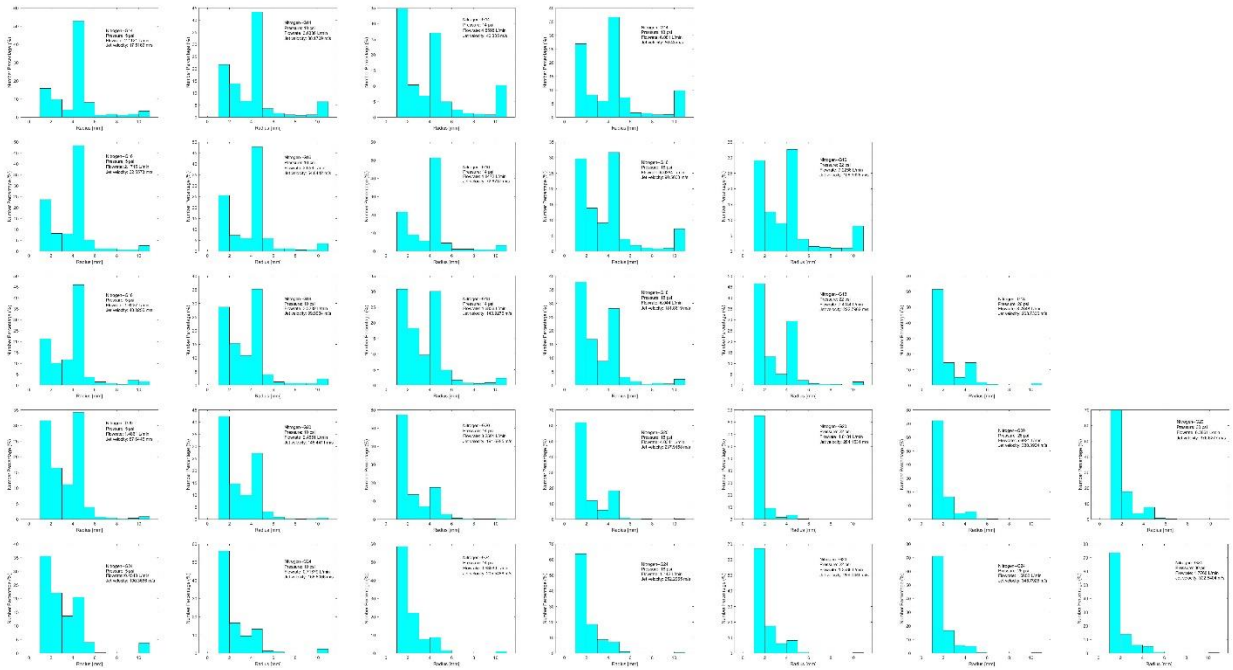

Fig. 4.10 Bubble number percentage histogram for Nitrogen gas with all needles and flowrates.

All bubble number percentage histograms for both nitrogen and methane under different testing conditions such as needle gauge numbers, pressures, flowrates, and jet velocities are compiled in Fig. 4.9 and Fig. 4.10. Generally speaking, the bubble behaviors for these constant flow cases are complicated and unpredictable. As can be seen from the recorded movies, the formations of bubbles involved highly dynamic processes, such as coexisting bubbles and gas plume that are detached from the needle, distorted and non-spherical bubbles, coalescences (inter-bubble contact to form large bubble), fragmentation (generating small bubbles

from large one), and vortex and turbulence. Detailed discussions can be found in the literature (Leighton, 1994). The results reveal the difficulties and complexities of interpreting the bubble number distribution at a high flowrate. To further analyze the above observations and gain better understanding of the underlying physics, more systematical experiments need to be designed and conducted.

4.4 Conclusion and Summary for acoustic bubble modeling

The acoustic behaviors of bubbles caused by oil leakages were studied in a laboratory under controlled conditions, such as flow rate, types of oil leakages, crack sizes, and gases. Specifically, two types of oil leakages were simulated: a few bubble case for oil seepage from sea-floor and the constant flow case for the situation of broken wellheads or pipelines. For a few bubble case, the resonant frequency obtained from the frequency spectrum was proportional to the negative one third of the needle diameter and inversely proportional to the bubble radius, in agreement with the theoretical predications. For the constant flow case, the total energy of power spectrum increased with the flow rate and jet velocity. After the analysis on the experiment data and theories, we found that the total energy is proportional to the jet velocity, bubble generation rate and the time. We further examine the bubble size distribution, and we found that for a specific needle, the higher the pressure, the more proportion of relatively smaller radii bubbles (the more proportion of sound signal of high frequency) are generated, and for different needles, the smaller the needle diameter, the more proportion of relatively smaller radii bubbles are generated. The bubble population histograms including the bubble number distribution and the number percentage distribution are also presented. Our work on the characterization of bubble leakage will help further bubble detections in more complex environments such as in oceans.

5. Localization

For **Task 3**, we successfully implement two different types of localization methods to localize the source position of bubbles: 1) TDOA-based localization, 2) Spectra ratio-based localization. The efforts were made for using the direction of arrival (DOA)-based localization method.

5.1 Water Tank Model

To illustrate the localization implementation of the leakage point in an experimental environment using a water tank, we first show the setup as in Fig. 5.1. The x, y, and z axes are parallel to the orthogonal walls of the tank, with the first two axes being in the horizontal plane and the last being the vertical direction. The dimensions of the water tank are noted as L_x, L_y, and L_{zt}, respectively, where $L_{zt} = 0.15\,\mathrm{m}$ corresponds to the water surface of the tank. In Table 5.1, h represents the thickness of the walls, and L_z represents the water height. As shown in Fig. 5.2, the bubbles generation system generates the bubbles. We randomly choose seven different leakage points (S1~S7) as the possible source position. For the localization purpose, we have tried two different types of receiver hydrophone arrangements: (1) scattered hydrophones, with seven hydrophones (CH1~CH7) randomly placed in the tank; and (2) hydrophone arrays, with total of five arrays (Array1~Array5) and each array has 4 hydrophones placed in a line either vertical or horizontal., Arrays 1, 2 and 3 are vertical arrays and Arrays 4 and5 are horizontal arrays. Hydrophones in (1) and arrays in (2) are randomly placed in the water tank, surrounding the bubble sources. The density and corresponding acoustic speed in the water tank wall, water and air are listed in Table 5.2.

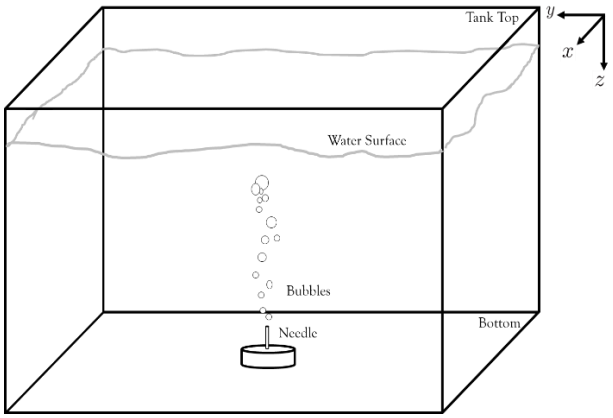

Fig. 5.1 A drawing of the water-filled tank with bubbles generated by the bubbles generation system

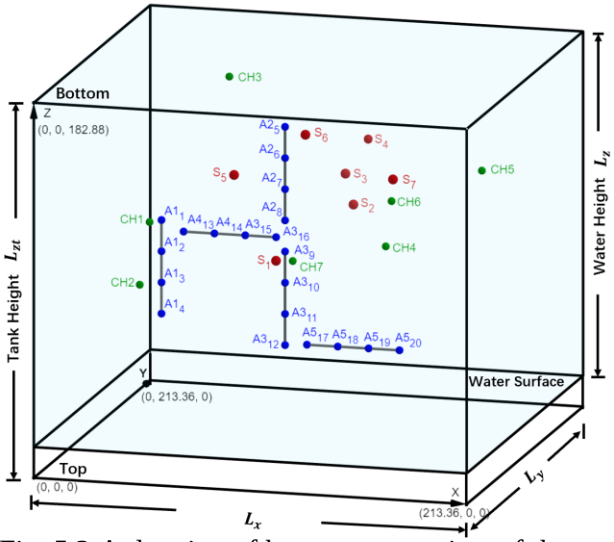

Fig. 5.2 A drawing of bottom to top view of the water tank. Green dots are scattered hydrophone. Blue dots are belonging to hydrophone arrays. Red dots are bubbles source positions.

Table 5.1 Water tank dimensions and thickness

[cm]	L_x	L_y	L_{zt}	L_z	h
Tank dimension	213.36	213.36	182.88	167.88	2.54

Table 5.2 Water tank dimensions and thickness

	c [m/s]	ρ [kg/m^3]
Wall (Lucite)	2690	1180
Liquid (water)	1500	1000
Air	340	1.225

5.2 TDOA-based Localization Algorithm

5.2.1 Time Difference of Arrival (TDOA) Estimation by the First-of-Arrival

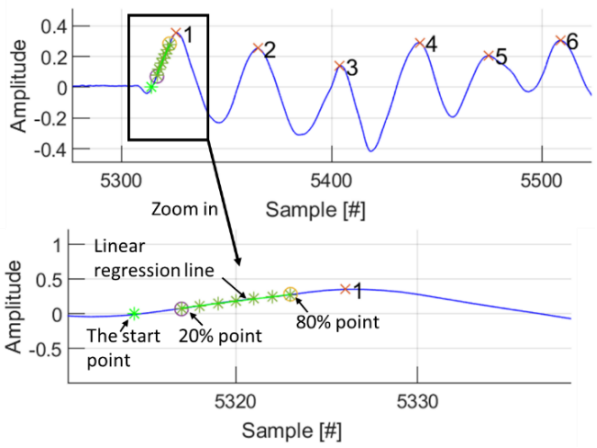

Fig. 5.3 Time delay estimation by first of arrival

As shown in Fig. 5.3, the received signal is shown as the "blue" curve recorded by a receiver hydrophone. We could find all the peaks of the received signal if the signal-to-noise ratio is larger enough. Assume that the first peak has coordinate (a, b). We define the 80% (or 20%) point as the point staying on the "blue" curve whose amplitude (i.e., the y-coordinate) is 80% (or 20%) of the value b and whose x-coordinate is less than a. By the linear regression for the points on the "blue" curve between the 20% point and the 80% point, we obtain the "green" line in Fig 5.3. The intersection point between the "green" line and the x-axis (i.e., the time domain), is defined as the first arrival point of the received signal. Repeating the above process for all received signals, we can find all the first arrival points. By finding the differences of the x-coordinates of those first arrival points pairwise, we can obtain the TDOAs between any two signals received at different hydrophones.

5.2.2 TDOA-based Localization Algorithm

Define the distance between the source and the i-th receiver hydrophone as r_i. The distance difference between r_i and r_1 is:

$$r_{\mathrm{TDOA},i} = t_{i1} \cdot c, \tag{5.1}$$

where t_{i1} is the time difference of the arrivals (TDOA) between the time of the source to receiver i and to receiver 1, which is estimated by the first-of-arrival method (section 5.2.1). c is the propagation speed of the acoustic signal in the water.

As shown in Fig. 5.4, given a fixed t_{i1}, Eq. **Error! Reference source not found.**) defines a hyperbola on which the emitting source lies. The target source location is given by the intersection of at least two hyperbolas. In the presence of disturbance, we estimate the source position from a set of hyperbolic equations converted from the TDOA measurements.

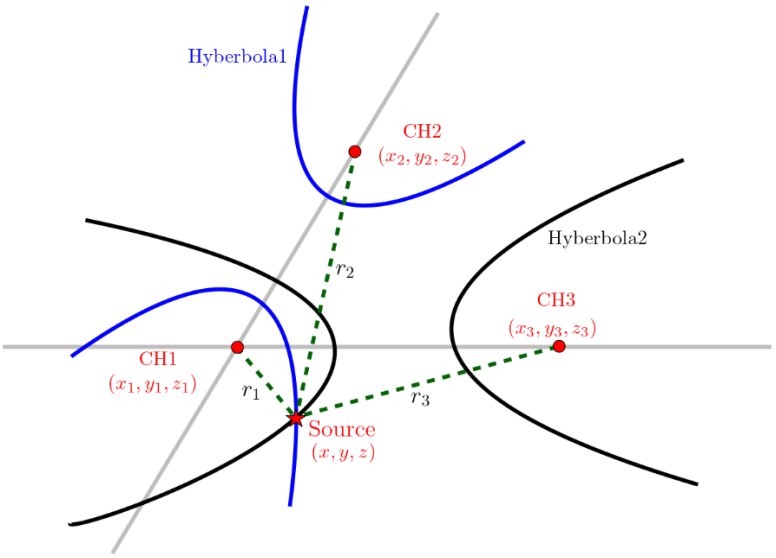

Fig. 5.4 2D hyperbolic localization Hydrophone CH1, CH 2 & CH 3 are Foci of Hyperbolas

The range difference measurements deduced from the TDOAs are modeled as

$$r_{\mathrm{TDOA},i} = r_{i1} + n_{\mathrm{TODA},i}, i = 2, \ldots, \mathrm{M}, \tag{5.2}$$

where

$$r_{i1} = r_i - r_1 = \sqrt{(x - x_i)^2 + (y - y_i)^2 + (z - z_i)^2} - \sqrt{(x - x_1)^2 + (y - y_1)^2 + (z - z_1)^2},$$

and source coordinate is $\mathbf{x} = (x, y, z)$, and the i-th receiver coordinate is (x_i, y_i, z_i). $n_{\mathrm{TODA},i}$ is the range difference error in $r_{\mathrm{TDOA},i}$, which is caused by the disturbance and distortion along the propagation path, and the noise at the hydrophone.

The source localization problem based on TDOA measurements is to estimate $\mathbf{x}$ given $\{r_{\mathrm{TDOA},i}\}$, $i = 2, \ldots, \mathrm{M}$. We implement two different methods to solve this localization problem:1) LLS method, 2) NLS with Gauss-Newton Method.

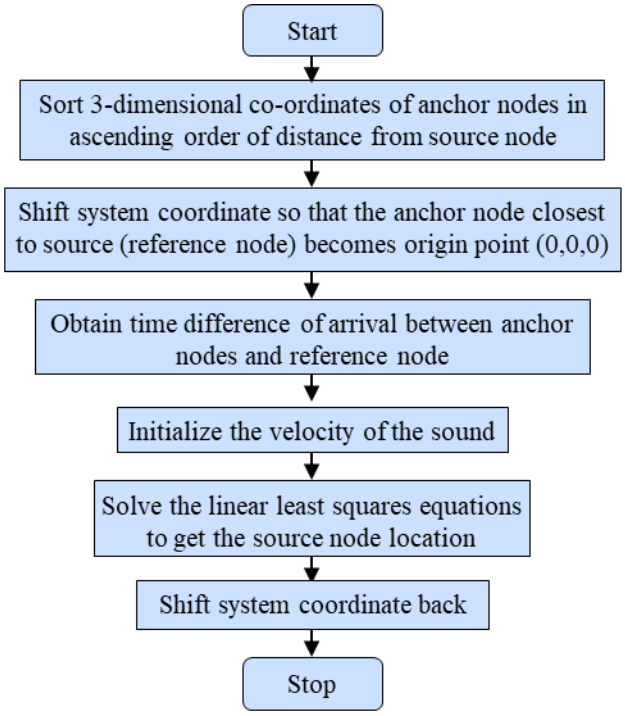

Fig. 5.5 The flowchart for Linear Least Square Estimation (LLSE)

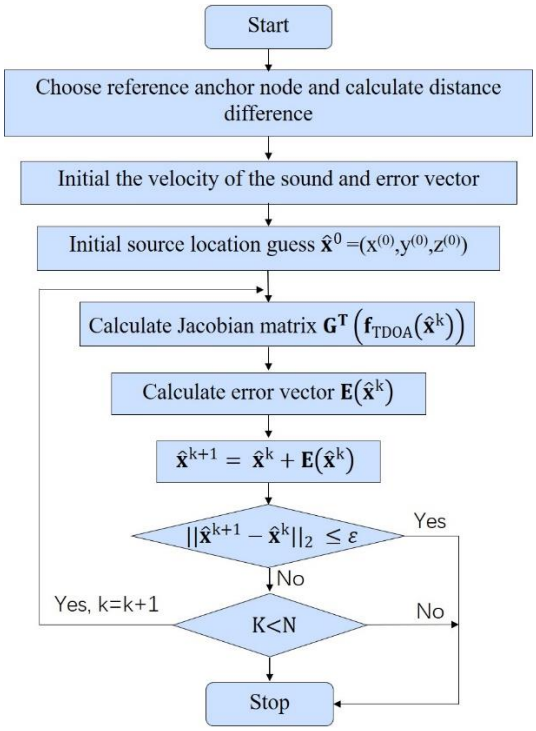

Fig. 5.6 The flowchart for NLS with Gauss-Newton estimation

LLS Method[1]-[3] The flowchart of the LLS (Linear Least Square) algorithm is shown in Fig. 5.5. The basic idea of the LLS approach is to reorganize the nonlinear expressions of Eq. (5.2) into a set of linear equations in $\mathbf{x}$ with zero-mean disturbances, assuming that the measurement errors are sufficiently small, and the position is then estimated by using the ordinary LS technique.

Rearrange the terms of Eq. () to get the following,

$$\mathbf{Hx} = r_1\mathbf{c} + \mathbf{d}, \tag{5.3}$$

where $\mathbf{H} = \begin{bmatrix} x_2 & y_2 & z_2 \\ \cdots & \cdots & \cdots \\ x_{\mathrm{M}} & y_{\mathrm{M}} & z_{\mathrm{M}} \end{bmatrix}, \mathbf{x} = \begin{bmatrix} x \\ y \\ z \end{bmatrix}, \mathbf{c} = \begin{bmatrix} -r_{\mathrm{TDOA},2} \\ \cdots \\ -r_{\mathrm{TDOA,M}} \end{bmatrix}, \mathbf{d} = \frac{1}{2}\begin{bmatrix} K_2^2 - r_{\mathrm{TDOA},2} \\ \cdots \\ K_{\mathrm{M}}^2 - r_{\mathrm{TDOA,M}} \end{bmatrix}, K_i^2 = x_i^2 + y_i^2 + z_i^2.$

To solve for $\mathbf{x}$, Eq. (5.3) is arranged into the following form by the least square method:

$$\mathbf{x} = r_1\mathbf{cH^{-1}} + \mathbf{dH^{-1}}, \tag{5.4}$$

with constraint $r_1 = \sqrt{(x - x_1)^2 + (y - y_1)^2 + (z - z_1)^2}$. $\mathbf{H^{-1}}$ is the pseudo-inverse of H.

There are mainly three advantages of the LLS estimator: (1) Global solution is guaranteed. (2) Simple and computationally efficient. (3) Noise statistics are not needed. However, its accuracy is generally low.

NLS with Gauss-Newton Method[4] To increase the accuracy of localization, we also implement the NLS

(nonlinear least square) method. The flowchart of its whole procedure is shown in Fig. 5.6. The nonlinear methodology attempts to find the source location directly from Eq. (), which is the conceptual difference from the linear method. The global convergence of the nonlinear estimator may not be guaranteed because their optimization cost functions are multimodal. The main advantages of this estimator are: (1) Accuracy is generally high. (2) Noise statistics are not needed.

The NLS approach minimizes the LS cost function directly constructed from Eq. (). The NLS cost function for TDOA-based positioning, is denoted by,

$$J_{\mathrm{NLS,TDOA}}(\tilde{\mathbf{x}}) = \left(\mathbf{r}_{\mathrm{TDOA}} - \mathbf{f}_{\mathrm{TDOA}}(\tilde{\mathbf{x}})\right)^{\mathrm{T}} (\mathbf{r}_{\mathrm{TDOA}} - \mathbf{f}_{\mathrm{TDOA}}(\tilde{\mathbf{x}})), \tag{5.5}$$

where

$$\mathbf{r}_{\mathrm{TDOA}} = \left[r_{\mathrm{TDOA},2}\ r_{\mathrm{TDOA},3} \cdots r_{\mathrm{TDOA},L}\right]^T,$$

$$\mathbf{f}_{\mathrm{TDOA}}(\tilde{\mathbf{x}}) = \begin{bmatrix} \sqrt{(\tilde{x}-x_2)^2+(\tilde{y}-y_2)^2+(\tilde{z}-z_2)^2} - \sqrt{(\tilde{x}-x_1)^2+(\tilde{y}-y_1)^2+(\tilde{z}-z_1)^2} \\ \cdots \\ \sqrt{(\tilde{x}-x_{\mathrm{M}})^2+(\tilde{y}-y_{\mathrm{M}})^2+(\tilde{z}-z_{\mathrm{M}})^2} - \sqrt{(\tilde{x}-x_1)^2+(\tilde{y}-y_1)^2+(\tilde{z}-z_1)^2} \end{bmatrix}$$

The result of the NLS position estimation is $\tilde{\mathbf{x}}$, which corresponds to the smallest value of $J_{\mathrm{NLS,TDOA}}(\tilde{\mathbf{x}})$; that is,

$$\hat{\mathbf{x}} = \arg\min_{\tilde{\mathbf{x}}} J_{\mathrm{NLS,TDOA}}(\tilde{\mathbf{x}}), \tag{5.6}$$

Finding $\hat{\mathbf{x}}$ is not a simple task as there are local minima apart from the global minimum in the 3-D space of $J_{\mathrm{NLS,TDOA}}(\tilde{\mathbf{x}})$. An iterative algorithm starting from an initial position is usually used to find a solution. If the initial position, denoted by $\hat{\mathbf{x}}^0$, is not far away from $\mathbf{x}$, it is expected that $\hat{\mathbf{x}}$ can be found in the iterative procedure. We use the Gauss-Newton method for the local search. For the Gauss-Newton method, the updating rule is

$$\hat{\mathbf{x}}^{\mathrm{k+1}} = \hat{\mathbf{x}}^{\mathrm{k}} + \mathbf{E}\left(\hat{\mathbf{x}}^{\mathrm{k}}\right), \tag{5.7}$$

where $\mathbf{E}\left(\hat{\mathbf{x}}^{\mathrm{k}}\right) = \left(\mathbf{G}^{\mathbf{T}}\left(\mathbf{f}_{\mathrm{TDOA}}\left(\hat{\mathbf{x}}^{\mathrm{k}}\right)\right)\mathbf{G}\left(\mathbf{f}_{\mathrm{TDOA}}\left(\hat{\mathbf{x}}^{\mathrm{k}}\right)\right)\right)^{-1}\mathbf{G}^{\mathbf{T}}\left(\mathbf{f}_{\mathrm{TDOA}}\left(\hat{\mathbf{x}}^{\mathrm{k}}\right)\right)(\mathbf{r}_{\mathrm{TDOA}} - \mathbf{f}_{\mathrm{TDOA}}(\hat{\mathbf{x}}^{\mathrm{k}}))$,

and $\mathbf{G}^{\mathbf{T}}\left(\mathbf{f}_{\mathrm{TDOA}}\left(\hat{\mathbf{x}}^{\mathrm{k}}\right)\right)$ is the Jacobian matrix of $\mathbf{f}_{\mathrm{TDOA}}\left(\hat{\mathbf{x}}^{\mathrm{k}}\right)$ computed at $\hat{\mathbf{x}}^{\mathrm{k}}$; k is the iteration number.

Starting with $\hat{\mathbf{x}}^0$, the iterative procedure of Eq. (5.7) is terminated according to a stopping criterion, which indicates convergence. Typical choices of stopping criteria include the maximum number of iterations (N) and error $||\hat{\mathbf{x}}^{\mathrm{k+1}} - \hat{\mathbf{x}}^{\mathrm{k}}||_2 < \varepsilon$, where ε is a sufficiently small positive constant.

5.2.3 TDOA Localization Algorithm Results

Table 5.3 Scatter receivers coordinates

[cm]	x	y	z
CH1	49.5	29.5	121.5
CH2	26.5	100	75
CH3	54	171	155
CH4	131	159	81
CH5	189.5	111	139
CH6	163.5	45	122
CH7	98	119	130

Sources S1 and S2 emit electrical tone burst signals; sources S3 and S4 emit pulse bubble signals generated by a small diameter needle so that the bubble power is high, leading to easily distinguished first of arrivals. The coordinates of scatter receiver hydrophones are listed in Table 5.3. TDOAs are estimated by the first-of-arrival method. As we can see from Table 5.4, LLSE and NLS approaches could effectively estimate the

source positions. The largest RMSE is smaller than 6cm for electric signals, and is smaller than 4.5cm for bubble signals.

Table 5.4 Sources position estimation using TDOA method

Sources	Signal Type	True Location (cm)	Estimated Location (cm)		RMSE (cm)	
			LLSE	NLS	LLSE	NLS
S1	Electric	(89.8, 66.3, 121.0)	(88.70, 68.92, 112.40)	(89.62, 70.70,111.96)	5.24	5.82
S2	Electric	(177.0, 74.5, 141.5)	(175.53, 78.05, 138.10)	(174.90, 79.01,137.59)	2.96	3.65
S3	Bubble	(139.8, 52.5, 145.5)	(137.87, 52.70, 139.66)	(138.49, 50.93,142.34)	3.54	2.16
S4	Bubble	(136.0,112.5,140.0)	(133.40,115.50,146.20)	(136.30,115.60,145.60)	4.25	3.70

5.3 The efforts for DOA-based Localization

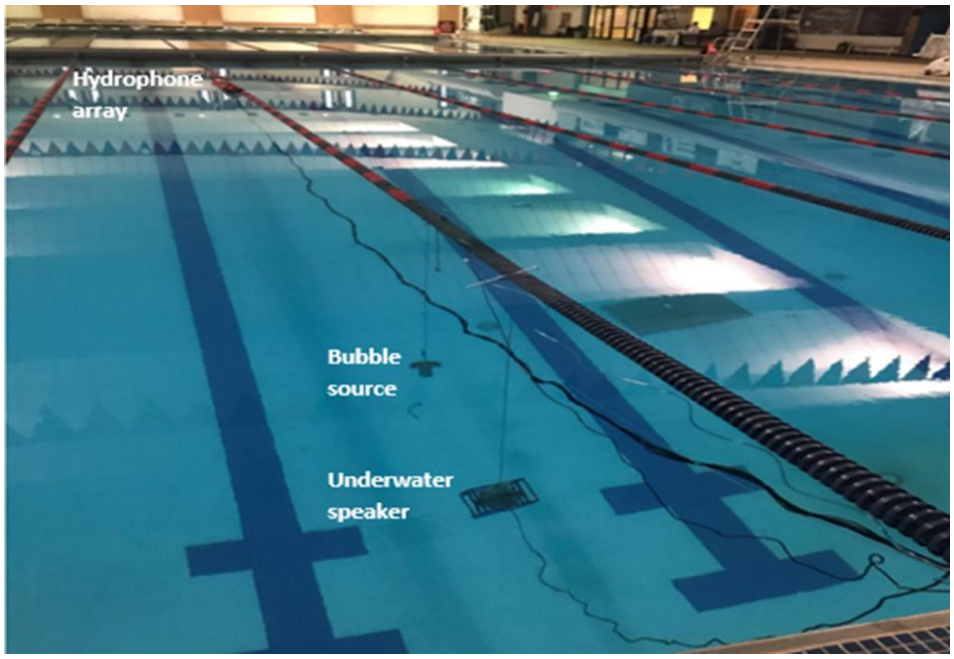

Fig. 5.7 The swimming pool test

In 2019, we focused on the study and experimentation of localization through Direction of Arrivals (DOA) using hydrophone arrays. In the field, for an oil leakage source, the underwater sound will be continuously generated. In this situation, it is difficult to determine the first arrival of the oil leakage sounds as we did for TDOAs before, and it is more desirable to study DOA-based localization methods.

Two sub-tasks were carried out. First, with known DOA information, we have successfully implemented an optimization method that can determine the source position in 3D space by combining multiple 1D DOA information. This implementation is important because we only have DOA information from 1D linear hydrophone arrays in current experimental environment. Second, we concentrated on the determination of DOA via linear hydrophone arrays. The array used in experiment consists of eight equally spaced hydrophones. Four hydrophone arrays were positioned at different locations to form a network. Instead of using two oscilloscopes (eight channels) as the data acquisition device (Figure 4) in 2018, a 32 channel simultaneous data acquisition board was used (Figure 5). Several localization algorithms using the DOAs were developed and tested, including generalized cross-correlation with phase transform (GCC-PHAT) and

subspace-based MUSIC algorithms. However, when we tested the DOA-based methods in the water tank, several difficulties emerged, such as (1) multipath and reverberation, i.e. the sounds reflected from the wall, bottom, and surface of the water tank in all directions and (2) near field effect, i.e. non-paralleled wave propagation. Efforts were made to (1) suppress the multipath/reverberation by adding a layer of artificial turf around the water tank and putting sound absorption foams on the top of water surface and (2) compensate the near effects in the algorithms. Despite of these efforts, we still cannot obtain a reliable DOA.

Realizing the limitations of the small water tank, we moved our test site to a swimming pool (Fig. 5.7) in the Recreation Center (Turner Center) of the University of Mississippi in an attempt to achieve far-field condition. The deepest part of the pool has a size of 22.9 m × 20.1 m × 3.96 m.

We re-constructed the hydrophone array by mounting the hydrophones with an equal separation of 15.2 cm in a rigid frame to improve equal spacing requirement (Fig. 5.8) since this requirement is very sensitive to DOA measurements.

Fig. 5.8 The hydrophone array

We also conducted a hydrophone calibration test (Fig. 5.9) to confirm the consistency among different hydrophones.

Fig. 5.9 The calibration of hydrophone array

Both vertical and horizontal hydrophone arrays were employed in the swimming pool tests. In order to overcome the ambient noises, a powerful underwater speaker (LuBelle Labs, Portable LL916C/H) was used as a controllable source. Tone burst and chirp signals were applied to excite the speaker.

However, these indoor measurements encountered some adverse issues, including severe noise generated from a swimming pool filtration pump, air conditioners of the building, and nearby machinery, as well as significant multipath/reverberation effects. Due to the outbreak of Covid-19 in 2020, the swimming pool test was suspended.

In this case, we moved our localization test back to the water tank. This time, we implemented a different localization approach that was not planned by the initial proposal. Instead of using the DOAs-based methods that require acoustic propagation in a free field or in an anechoic environment, a Green's function method was adapted to deal with highly multipath/reverberation environment and near field conditions of the water tank, as described in the following section.

5.4 Spectra Ratio-based Localization Algorithm

5.4.1 Water Tank Channel Models and Spectra Ratio-based Localization Algorithm

The water tank is a highly reverberant acoustic environment, exhibiting very strong and narrow resonances [5][6]. To deal with the highly reverberating environments, a set of Green's functions consisting of all frequency responses between each point source and each position of the receiver hydrophone must be known either experimentally or by analytical models [7]-[9]. Here, we use a new analytical water tank acoustic channel model to estimate the tank channel response, denoted by $G(\vec{r}_n, \vec{r}_s, \omega)$, that is, the pressure field at the receiver position $\vec{r}_n = (x_n, y_n, z_n)$, corresponding to a harmonic (ω) point source located at $\vec{r}_s = (x_s, y_s, z_s)$.

We implemented three different water tank channel models in the following.

1) M1 (Dirichlet Model)[10] is the most commonly used analytical approach relying on standard eigenvalue solutions that assume the acoustic pressure decays to zero at the walls, the bottom, and the free surface of the "brick" of liquid. That is, the six surfaces are assumed to be perfect sound reflectors and the damping due to the numerous reflections per unit time is neglected. Actually, this "zero order" approximation leads to infinite values for the modal quality factors; this is unfortunately not physically realistic.
2) M2 (Including Leakage Through the Walls Model) [10] is a method improved by considering the boundary conditions at the upper surface of the liquid (water) and at the walls of the tank (including the tank floor) corresponding to non-zero (but small) acoustic pressure amplitudes associated with a particle movement that exists even close to the wall. The effects of the lossy and reacting vibrations of the walls on each acoustic mode in the brick of water (which include the energy leakage outside in the air) are specified by the small modal specific impedances. That is, the M2 model expresses both the acoustic leakage through the walls (lossy and reacting walls) and the modal solutions for the sound pressure field and the acoustic velocity field.
3) Proposed (Proposed New Water Tank Model) is a method further considering the real setup of bubble source experiments. The M2 model considers the five walls to be surrounded by air, including the bottom wall. However, in the measurement conditions, the water tank is directly supported by the ground. This inaccuracy of the boundary conditions at the bottom wall can lead to lower precision of the localization algorithm in the z-direction. The proposed model is developed to solve this problem, by considering z-direction as a perfect sound reflector.

Based on the water tank channel model, we utilize the spectra ratios-based method[11] to localize the location of pipe leakage which induces the bubbles. The framework of spectra ratio-based localization is shown in Fig. 5.10. The key idea is the following:

The spectrum $P_n(\omega)$ of the sound pressure recorded with the n-th hydrophone can be expressed as

$$P_n(\omega) = G(\vec{r}_n, \vec{r}_s, \omega)X(\omega), \tag{5.8}$$

where $G(\vec{r}_n, \vec{r}_s, \omega)$ is the Green's function, and $X(\omega)$ is the spectrum of the sound pressure emitted by the bubbles source located at $\vec{r}_s$.

The spectra ratio $S_{m,n}(\vec{r}_s, \omega)$ is defined as a criterion for the localization algorithm:

$$S_{m,n}(\vec{r}_s,\omega)=\frac{G(\vec{r}_m,\vec{r}_s,\omega)P_n(\omega)}{G(\vec{r}_n,\vec{r}_s,\omega)P_m(\omega)},\ \text{where } n\neq m. \tag{5.9}$$

In a perfect case where the Green's functions perfectly describe the real water tank, the received spectrum at position of the n-th hydrophone will perfectly match $P_n(\omega)$, the spectra ratio $S_{m,n}(\vec{r}_s,\omega)$ is equal to 1. In a real-world application the closer the ratio $S_{m,n}(\vec{r}_s,\omega)$ is to one, the higher the probability that the candidate source position is the real source position. To find the location estimate, we calculate the root mean square of $S_{m,n}(\vec{r}_s,\omega)$ in dB scale as

$$\sigma_{m,n}(\vec{r}_s)=\sqrt{\frac{1}{\omega_2-\omega_1}\int_{\omega_1}^{\omega_2}\left(20\,log_{10}\left|S_{m,n}(\vec{r}_s,\omega)\right|\right)^2 d\omega}, \tag{5.10}$$

where ω_1 and ω_2 are chosen to cover the frequency band from 600Hz to 2kHz. Finally, we use the detection factor $DF(\vec{r}_s)$ to consider the effects of all seven hydrophones as

$$DF(\vec{r}_s)=\frac{1}{\prod_{m=1}^{6}\prod_{n=m+1}^{7}\sigma_{m,n}(\vec{r}_s)}. \tag{5.11}$$

The position estimation result of the spectra ratio approach is $\vec{r}_s$ which maximize detection factor (DF).

Algorithm Framework of spectra ratio-based localization

Input:

1: The water tank and grids dimension, receivers' location and number

2: The recorded signal by receivers, $p_i, i=1,\dots,7$

Output:

3: Calculate three different model's* Green's functions dictionary with help of step1, $G(\vec{r}_i,\vec{r}_s,\omega)$

4: Transfer p_i to frequency domain $P_i(\omega)$ with interested frequency range 600Hz to 2KHz.

5: Calculate spectra ratio $S_{m,n}(\vec{r}_s,\omega)$ with help of $G(\vec{r}_i,\vec{r}_s,\omega)$ and $P_i(\omega)$

6: calculate the rms of $S_{m,n}(\vec{r}_s,\omega)$ in dB scale

7: Calculate detection factor of all receivers with help of step 6

8: Estimation result is $\vec{r}_s$ which maximize detection factor (DF)

9: **return** $\vec{r}_s$

*Three models are M1, M2 and Propose, respectively.

Fig. 5.10 The framework of spectra ratio-based localization algorithm

5.4.2 Spectra Ratio-based Localization Results

Table 5.5 The coordinates of the scattered receiver hydrophones positions used during the localization

[cm]	x	y	z
CH1	49	30	121
CH2	26	97.5	74
CH3	52	165	162
CH4	131	158	85.5
CH5	191	111	136.5
CH6	164.5	44	135
CH7	94	125	83.5

Table 5.6 The coordinates of the different source positions used during the localization

[cm]	x	y	z
S4	146	112	148
S5	71	103	129
S6	102	118.5	147
S7	146.5	113.5	129

In the experiment, there are seven receiver hydrophones whose coordinates are listed in Table 5.5. To verify

the effectivity of the algorithm, we also randomly select 4 different positions listed in Table 5.6 as the bubble source.

The searching for the most probable source location $\vec{r}_s = (x_s, y_s, z_s)$ that maximizes $DF(\vec{r}_s)$ can be done by the computation of a dictionary of power ratio in a given grid. Here, we divide the tank into $10 \times 10 \times 10$ grids. The grid axes are listed in **Error! Not a valid bookmark self-reference.**. For each grid, seven sets of $G(\vec{r}_n, \vec{r}, \omega), n = 1, \ldots, 7$ between the hydrophone n position $\vec{r}_n = (x_n, y_n, z_n)$ and each point $\vec{r} = (x, y, z)$ in the grid are computed.

Table 5.7 Water tank dimension grid ($10 \times 10 \times 10$)

No.	1	2	3	4	5	6	7	8	9	10
x	0.107	0.32	0.533	0.747	0.96	1.173	1.387	1.6	1.814	2.027
y	0.107	0.32	0.533	0.747	0.96	1.173	1.387	1.6	1.814	2.027
z	0.084	0.252	0.42	0.588	0.755	0.923	1.091	1.259	1.427	1.595

Experiment 1 Aim: To verify the feasibility of the spectra ratio-based localization algorithm.

The data used is Tank-20-07-29-08-08-47-S7-bubble pulse-20 kHz, down sampled the sampling frequency (Fs) to 10KHz. The signal segment used is from the 2e3-th sample to the 4.3e4-th sample. Coordinates of the seven receiver hydrophones are listed in Table 5.6.

Table 5.8 S7 source position is estimated by the proposed new water tank model

	Model	**X [m]**	**Y [m]**	**Z [m]**	**RMSE[m]**
S7 Bubble True Coordinate		1.465	1.135	1.29	
Tank-20-07-29-08-08-47-S7-bubble pulse-20 kHz	Proposed	1.600	1.173	1.091	0.141

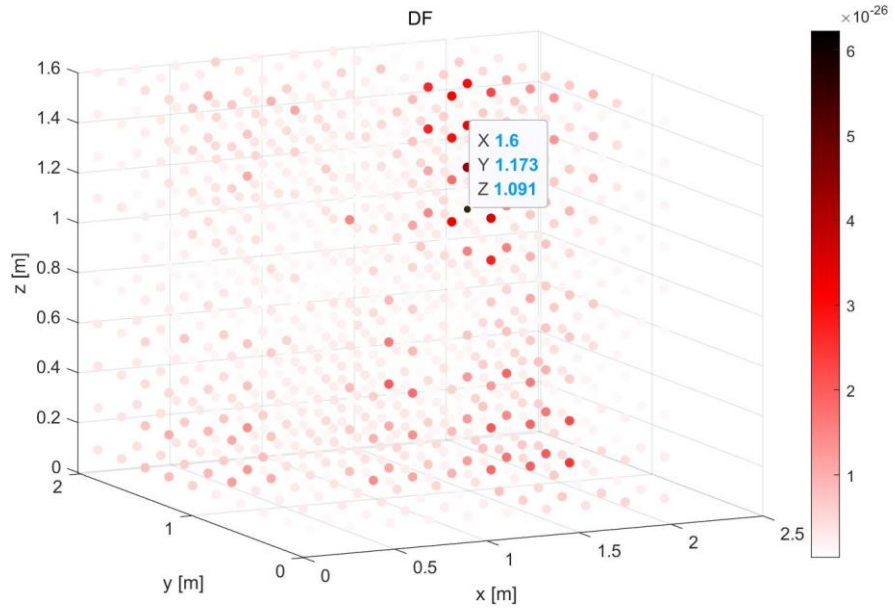

Fig. 5.11 The detection factor (DF) in 3D space

As shown in Fig. 5.11, since we divide the water tank into $10 \times 10 \times 10$ grids, there are 1000 possible

source points, that is 1000 DF values. The possible source coordinates that make DF the maximum will be decided as the estimated source coordinates. In the 2D (x-y with z=1.091) plane as shown in Fig. 5.12, we can easily observe that the darkest point shows the x- and y-axis of the estimated source coordinate. From Table 5.8, we can see that the proposed method can effectively localize the position of the bubble source. For this estimate, the RMSE is 0.141m.

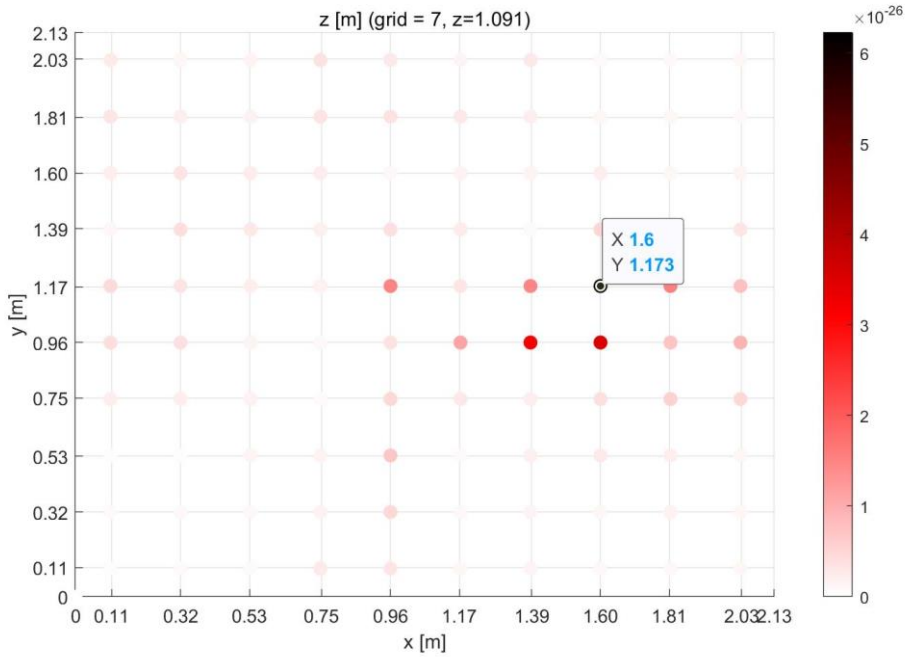

Fig. 5.12 The detection factor (DF) in 2D (x-y plane) space with z-axis is 1.09122m

Experiment 2 Aim**:** To verify the feasibility of using different part of recorded signals.

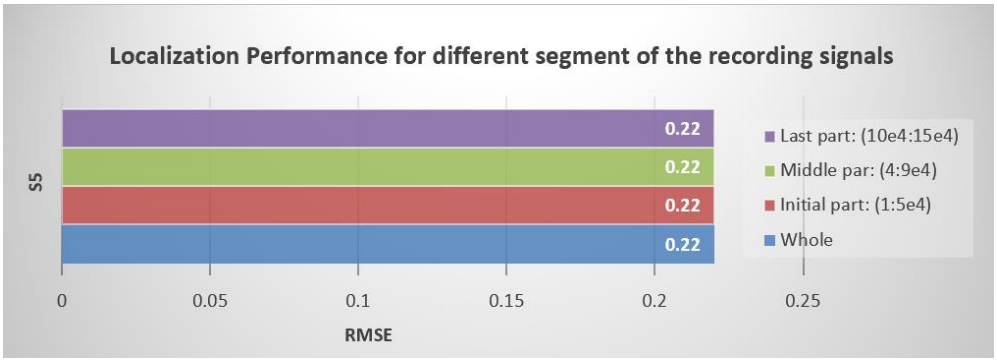

Fig. 5.13 Localization performance for different segment of the S5 continuous bubble

Since bubbles induced by the broken oil-pipe can be generated at any time and continuously, in practice, Sensed signal at hydrophones in any time period may be used for the localization purpose. Hence, we need to verify whether this algorithm still works when we randomly choose any part of the recording signal for localization. The localization performance for any three different segments of continuous bubbles at S5 position are listed in Table 5.9.

As we can see in Fig. 5.13, no matter which part of the recording signals is used, the estimation results of the source position are very close except tiny differences in the DF values.

Table 5.9 Estimated position with different segment of signals

	x [m]	y [m]	z [m]	RMSE[m]	$DF(\vec{r}_{\hat{s}})$	Segment of recording signals
S5	0.71	1.03	1.29			
Tank-20-07-10-08-16-27-S5-Bubble continuous-20 kHz	0.533	1.173	1.59	0.22	9.39E-26	Whole
	0.533	1.173	1.59	0.22	1.02E-25	Initial part: (1:5e4)
	0.533	1.173	1.59	0.22	9.57E-26	Middle par: (4:9e4)
	0.533	1.173	1.59	0.22	9.12E-26	Last part: (10e4:15e4)

Experiment 3 Aim**:** To verify whether the algorithm works for different sampling frequencies.

For the channel response model and spectra ratio-based localization algorithm, the sampling frequency used in data collection needs not to be as high as that used in the methods to distinguish the time difference of arrivals (TDOA). A sampling frequency in the Nyquist rate or slightly higher may still work for the spectra ratio-based method.

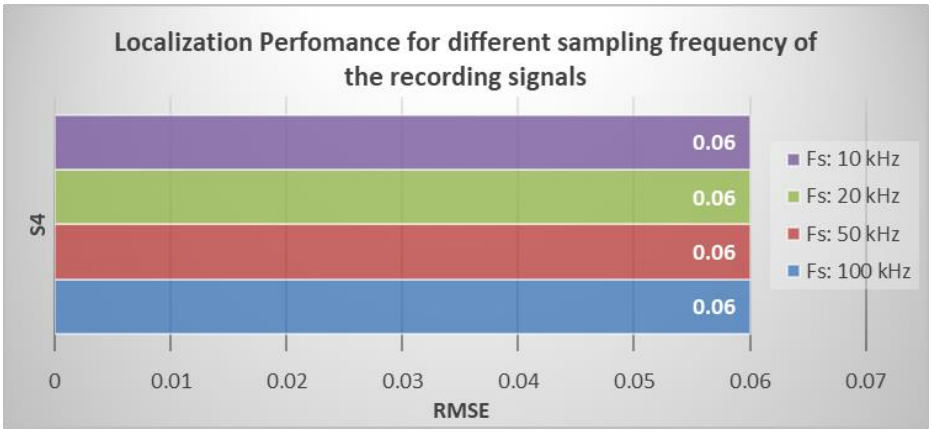

Fig. 5.14 Localization performance for different sampling frequencies of the S4 pulse bubble

Table 5.10 Estimated position with different sampling frequencies

	Fs [kHz]	X [m]	Y [m]	Z [m]	RMSE[m]
S4		1.46	1.12	1.48	
Tank-20-06-13-07-26-01-S4-Bubble pulse-200 kHz	100	1.39	1.17	1.43	0.06
	50	1.39	1.17	1.43	0.06
	20	1.39	1.17	1.43	0.06
	10	1.39	1.17	1.43	0.06

As shown in Table 5.10 and Fig. 5.14, we can see that no matter which sampling frequency is used (must be larger than two times of the original signal frequency), the estimated source positions will be the same.

Experiment 4 Aim**:** To study the performance of the algorithm with different number of hydrophone receivers

As shown in Fig. 5.15 and Table 5.11, even though the same number of receivers are used, for different combinations of the receivers, the localization results such as RMSEs may be different. In this case using CH1-2-4 has better performance than using CH1-2-3. The possible reasons may include: (1) Hydrophones 1-2-4 are better calibrated than other hydrophones; (2) The channel model are more accurate for channels 1, 2 and 4 than other channels due to the physical setup. It is observed that as the number of receivers increases, the localization performance in general is getting better, which is understandable as the effect of noise and turbulence can be smoothed by more number of receivers.

Table 5.11 Estimated position with different number of receivers and corresponding receivers' combination

Source	# of RXs (Combination)	Model	X [m]	Y [m]	Z [m]	RMSE[m]
S7			1.47	1.14	1.29	
Tank-20-07-29-08-06-36-S7-bubble continous-20 kHz (segment: 2e3 to 4.3e4)	3 (CH1,2,4)	Proposed	1.60	1.17	1.26	0.08
	3 (CH1-CH3)	Proposed	0.53	1.17	0.08	0.88
	5 (CH1-CH5)	Proposed	1.39	0.96	1.59	0.21
	7 (CH1-CH7)	Proposed	1.60	1.17	1.09	0.14

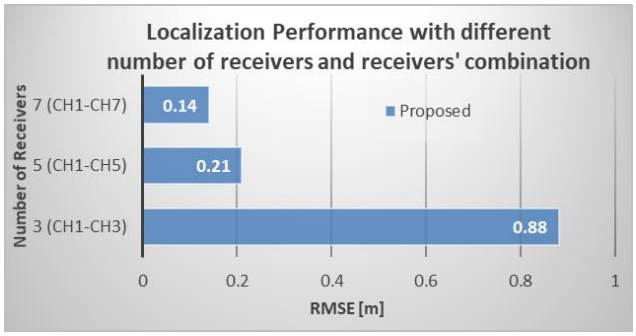

Fig. 5.15 Localization performance for different number of receivers and corresponding receivers' combination

Experiment 5 Aim: To test different positions of the bubble source and compare the localization results based on the three different channel models. Here, M1, M2 and "The proposed" stand for the 'Dirichlet Model', 'Including Leakage Through the Walls Model', and the 'Proposed New Water Tank model', respectively. The estimation results of four source positions, i.e., S4 to S7, are shown in Table 5.12. For each source position, there are two types of bubbles: pulse bubbles and continuous bubbles, being used for the test.

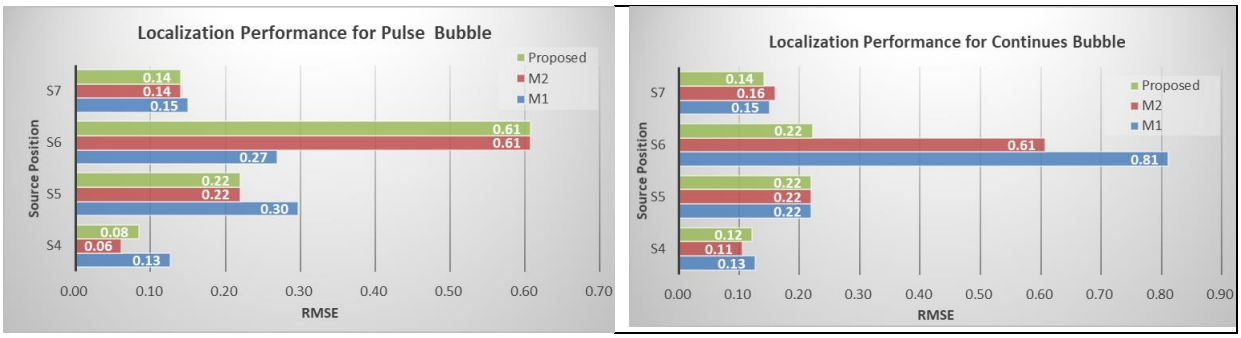

Fig. 5.16 Localization performance for Pulse Bubble and Continues Bubble source S4 to S7

As shown in Fig. 5.16, for continuous bubbles at S7 and continuous bubbles at S6, the proposed method has the best performance (with the smallest RMSE). For most cases, the proposed method and M2 method give the same localization results. However, it should be noted that the difference could still exist if more number of grids are used. However, using more number of grids increases the computational complexity drastically. For most cases, the M1 method has the worst performance, with the result of pulse bubble in S6 as an exception where the M2 and Proposed method have a poor estimate of the z-axis, even though the x- and y-coordinates estimates are more accurate than that by the M1 method.

Table 5.12 Estimated position and RMSE

Pulse Bubble	Model	X [m]	Y [m]	Z [m]	RMSE	Continous Bubble	Model	X [m]	Y [m]	Z [m]	RMSE
S4		1.46	1.12	1.48		S4		1.46	1.12	1.48	
Tank-20-06-13-07-26-01-Bubble-200 kHz	M1	1.60	0.96	1.43	0.13	Tank-20-07-09-07-47-41-S4-Bubble continuous-20 kHz	M1	1.60	0.96	1.43	0.13
	M2	1.39	1.17	1.43	0.06		M2	1.39	0.96	1.43	0.11
	Proposed	1.39	1.17	1.59	0.08		Proposed	1.39	0.96	1.59	0.12
S5		0.71	1.03	1.29		S5		0.71	1.03	1.29	
Tank-20-07-10-08-22-35-S5-Bubble pulse-20 kHz	M1	0.32	1.17	1.59	0.30	Tank-20-07-10-08-16-27-S5-Bubble continuous-20 kHz	M1	0.53	1.17	1.59	0.22
	M2	0.53	1.17	1.59	0.22		M2	0.53	1.17	1.59	0.22
	Proposed	0.53	1.17	1.59	0.22		Proposed	0.53	1.17	1.59	0.22
S6		1.02	1.19	1.47		S6		1.02	1.19	1.47	
Tank-20-07-28-07-14-51-S6-bubble pulse-20 kHz	M1	1.17	0.96	1.09	0.27	Tank-20-07-28-07-16-11-S6-bubble continous-20 kHz	M1	0.96	0.96	0.08	0.81
	M2	0.96	1.17	0.42	0.61		M2	0.96	1.17	0.42	0.61
	Proposed	0.96	1.17	0.42	0.61		Proposed	0.96	1.17	1.09	0.22
S7		1.47	1.14	1.29		S7		1.47	1.14	1.29	
Tank-20-07-29-08-08-47-S7-bubble pulse-20 kHz	M1	1.60	0.96	1.43	0.15	Tank-20-07-29-08-06-36-S7-bubble continous-20 kHz	M1	1.60	0.96	1.43	0.15
	M2	1.60	1.17	1.09	0.14		M2	1.39	0.96	1.09	0.16
	Proposed	1.60	1.17	1.09	0.14		Proposed	1.60	1.17	1.09	0.14

Experiment 6 Aim**:** To compare performance with different water tank grid dimensions

Table 5.13 Estimated position with different grid dimension for pulse bubble signal S6

Pulse Bubble	Grid	Model	X [m]	Y [m]	Z [m]	RMSE[m]
S6			1.02	1.19	1.47	
Tank-20-07-28-07-14-51-S6-bubble pulse-20 kHz	$10 \times 10 \times 10$ (Table 5.7)	M1	1.17	0.96	1.09	0.27
		M2	0.96	1.17	0.42	0.61
		Proposed	0.96	1.17	0.42	0.61
	$20 \times 20 \times 20$	M1	1.12	1.01	0.46	0.59
		M2	1.12	1.01	0.97	0.31
		Proposed	1.12	1.01	1.13	0.23

Table 5.14 Water tank dimension grid ($20 \times 20 \times 20$).

Grid No.	1.00	2.00	3.00	4.00	5.00	6.00	7.00	8.00	9.00	10.00
X	0.05	0.16	0.27	0.37	0.48	0.59	0.69	0.80	0.91	1.01
Y	0.05	0.16	0.27	0.37	0.48	0.59	0.69	0.80	0.91	1.01
Z	0.04	0.13	0.21	0.29	0.38	0.46	0.55	0.63	0.71	0.80
Grid No	11.00	12.00	13.00	14.00	15.00	16.00	17.00	18.00	19.00	20.00
X	1.12	1.23	1.33	1.44	1.55	1.65	1.76	1.87	1.97	2.08
Y	1.12	1.23	1.33	1.44	1.55	1.65	1.76	1.87	1.97	2.08
Z	0.88	0.97	1.05	1.13	1.22	1.30	1.39	1.47	1.55	1.64

As we can see from Table 5.13, with a smaller grid step, such as the $20 \times 20 \times 20$ water tank grid dimension (listed in Table 5.14), the localization result is more accurate by using M2 and the proposed model, where the proposed model gives us the smallest RMSE. However, for the M1 model, the performance is getting worse as compared to using a larger grid step. Since the Dirichlet model is not interpreting our experiment boundary condition properly, using more number of grids may induce a large error.

5.5 Discussion and Conclusion

The localization of the bubble acoustic source caused by oil leakages was studied in a laboratory environment under controlled conditions, such as flow rate, types of oil leakages, crack sizes and gases. In 2018, we utilized the first-of-arrival-based TDOA estimation and TDOA localization method to localize the bubble source position successfully. By applying the experiment data, the estimated bubble source position is highly accurate, and the RMSE for bubble source position is less than 4.5cm. In practice, however, this method has severe limitations due to two facts: 1) To save power, the receiver hydrophones record the signals intermittently, and it is possible that the first-of-arrival signal segments are missed. Therefore, it requires that the localization algorithm can use any part of the recorded signals as the input but not only the signal segments included the first arrival point. 2) To get the accurate TDOAs estimates, the first arrival point of the bubble source must have higher SNR to guarantee the first peak not being overwhelmed in the environment noise. In the real ocean environment, however, the SNR may be very low, which may lead to a huge error for the TDOAs estimation. Hence, different algorithms are needed to solve the localization problem.

In 2019, we implemented the GCC (Generalized cross correlation)[12] -based TDOAs estimation. It worked very well for simulation data, but failed when using the data collected in experiments. Analysis shows that the possible reasons are: (1) The bubbles source is not stationary random processes which is time-varying signal. It contradicts with the GCC assumption. (2) The water tank has a strong multipath effect which is

induced by the water surface and five walls. Multiple power comparable reflection paths lead to highly different shapes of the received signals whether those hydrophones are near to each other or not. We further implemented the hydrophone arrays-based spectral estimation techniques based on the DOA (direction of arrival), including beamforming[13], ESPRIT[15], MUSIC[14], Spatial Smoothing improved MUSIC[16], Improved Wideband Signal ISSM (Incoherent Signal Subspace Method) Algorithm[17]. All of those methods again failed when using the data collected in experiments, possible reasons are: (1) In the relative small water tank, the arrival directions at different sensors in one array cannot be considered as parallel that is assumed in these methods. (2) Subspace-based MUSIC algorithm is very sensitive to senor positions, gains, and phase errors, which requires high quality hydrophones and very precise calibration of them. (3) There is a severe multipath problem in the water tank, even though we improved the algorithm to make it can handle coherent signals, the maximum number of coherent signals is limited by the number of sensors (hydrophones) per array. In the water tank setup, 8 hydrophones per array was tried, which is still far less than the number of reflection paths which include those reflected from boundary walls/bottom/surface multiple times.

In 2020, to deal with the highly reverberating water tank acoustic environments, the analytical water tank channel model using Green's functions was developed. Utilizing this model together with the spectra ratio-based localization method, the bubble source positions are successfully located. It should be noted the current work is conducted in the water tank. To extend to a field environment such as the real sea, feasibility of all the above methods and their parameter spaces need additional research efforts.

6. Conclusion and Summary

A laboratory study to simulate hydrocarbon leakages was conducted under controlled conditions, such as pressures, flow rates, jet velocities, and crack sizes. Two types of oil leakages were tested to simulate oil seepages either from seafloors or from oil well and pipe-line breaches. Two types of gases were investigated: nitrogen and methane. The latter is the major component of natural gases. The bubble sounds were recorded by the passive hydrophones and transformed into frequency spectra through the fast Fourier transform for signal analysis. It was found that (1) the resonant frequency decreased nonlinearly with the diameter of needle and (2) the sound intensity in terms of the total energy increased with both the flow rate and the jet velocity. These observations are of significance for assessing the properties of oil leakages in terms of crack size, flow rate, and jet velocity. It was also found that oil leakage –induced underwater sounds was created predominantly by bubble oscillations rather than by jet streaming.

For the task of acoustic bubble modeling, we implemented the theory of bubble dynamics to analyze the data taken from the above experiments. We considered (1) the dependence of the resonant frequency on the size of crack, (2) the dependence of the sound intensity in terms of the total energy on the flow rate and jet velocity, and (3) the bubble size distribution. Several correlations between the oil leakage properties and acoustic responses were established and interpreted. The outcome of the modeling enhanced our understanding of the underlying mechanisms of bubble-induced sounds and will be applied to guide the assessment of the features of oil leakage from the recorded sound signals.

For the task of localization, the time difference of arrivals (TDOAs) determined from the first of arrival were used as input parameters for localization algorithms. Two types of algorithms were developed and tested: Linear Least Square Estimation (LLSE) and Nonlinear Least Square (NLS) Estimation. It was also found that the proposed DOA-based localization methods were not suitable for this small-scale water tank due to strong multipath, reverberation, and near field effects. To overcome these technique challenges, approach that was based on an analytical modeling the acoustic field of the water tank, i.e., the Green's function of the water tank, was developed and tested. The estimated locations using both the TDOA and Green's function techniques were in good agreement with the true source locations. It should be noted that the Green function method can only be used specifically for the water tank. For a more realistic situation

of oil spill, the conventional localization algorithms such as the TDOA-based, DOA-based and energy-based method, and other advanced algorithms such as neutral network, matched field processing (MFP) methods should be developed. In this case, a test site with a large area, like a lake or ocean, is needed. In the future, we are considering to use Sardis Lake, Oxford, MS, 12 miles away from the university campus, as our testing site. That will be the future research work for the next proposal.

Acknowledgements

This work was funded by The Gulf Research Program of the National Academy of Science under the Grant Award Number: 200008860

References

- Abbott, J.P., and R. Raspet, 2015, “Calculated wind noise for an infrasonic wind noise enclosure,” J. Acoust. Soc. Am. 138, 332
- Blewitt, G., 1997, “Basics of the GPS Technique: Observation Equations,” in Geodetic Applications of GPS, Swedish Land Survey
- Camilli, R., D.D. lorio, A. Bowen, C.M. Reddy, A.H. Techet, D.R. Yoerger, L.L. Whitcomb, J.S. Seewald, S.P. Sylva, and J. Fenwick, 2012, “Acoustic measurement of the Deepwater Horizon Macondo well flow rate”, PNAS, 109:20235-20239.
- Deepwater Horizon Study Group, 2011, “Final report on the investigation of the Macondo well blowout”, pages 126.
- Erol-Kantarci, M., Mouftah, H.T., and Oktug, S., 2011, “A Survey of Architectures and Localization Techniques for Underwater Acoustic Sensor Networks,” IEEE Communications Surveys & Tutorials, Vol. 13, No. 3, 487-502
- Juhasz, A., 2012, "Investigation: Two Years After the BP Spill, A Hidden Health Crisis Festers". The Nation.
- Leighton, T.G., 1994, “The acoustic bubble”, ISBN 0-12-441920-8 Academic Press Inc., London, NW1 7DX, San Diego, CA 92101
- Leighton, T.G., and A. Walton, 1987, “An experimental study of the sound emitted from gas bubbles in a liquid”, Eur. J. Phys. 8:98-104.
- Longuet‐Higgins, M., Kerman, B.R., Lunde, K., 1991. "The release of air bubbles from an underwater nozzle". The Journal of the Acoustical Society of America 89, 2014-2014.
- Lorio, D.D, 2017, “An inventory of natural seeps using archived acoustic backscatter data”, Gulf of Mexico Oil Spill & Ecosystem, Science Conference, 2017, New Orleans, LA.
- Lurton, X., 2002, “An introduction to underwater acoustics: principles and applications”, ISBN 3-540-42967-0 Springer-Verlag Berlin Heidelberg New York
- Mahajan, A., and Walworth, M., 2001, “3-D Position Sensing Using the Differences in The
- Manasseh, R., Riboux, G., Risso, F., 2008. “Sound generation on bubble coalescence following detachment”. International Journal of Multiphase Flow 34, 938-949.
- Minnaert, M.,1933, "On musical air-bubbles and the sound of running water", Philosophical Magazine, 16 (104): 235–248.
- Nasibullaeva, E. S. and I. S. Akhatov, 2013, “Bubble cluster dynamics in an acoustic field”, J. Acoust. Soc. Am. 133(6), 3727-3738.
- Niu, X., X. Li, and X. Yu, 2013, “A model to simulate the spreading of oil and gas in underwater oil spills”, proceddings of the 7th International Conference on Asian and Pacific Coasts (APAC 2013) Bali, Indonesia.
- Ouyang, R. W., and Wong, A K-S. 2012, “On Data Fusion for Parametric-Model-based Wireless Localization,” International Journal of Wireless Information Networks, 19:22-37
- Reddya, C.M., J. S., Areyb, J.S., Seewalda, S.P., Sylvaa, K.L., Lemkaua, R.K., Nelsona, C.A., Carmichaela, C.P., McIntyrea, J. Fenwickc, G.T., Venturad, B.A.S.V., Mooya, and R., Camillic, 2012, “Composition and fate of gas and oil released to the water column during the Deepwater Horizon oil spill”. Proceedings of the National Academy of Sciences of the United States of America, 109. 20229–20234, doi: 10.1073/pnas.1101242108
- Ribeiro, F. J. L., Pedroza, A. C., and Costa, L H. M., 2015, “Underwater Monitoring System For Oil Exploration Using Acoustic Sensor Networks,” Telecommun Syst. (2015) 58:91–106
- Riccardi, G., and E.D. Bernardis, 2016, “Dynamics and acoustics of a spherical bubble rsing under gravity in an inviscid liquid”, J. Acoust. Soc. Am., 140, 1488-1497.

- Tan, H-P., Diamant, R., Seah, W.K.G., and Waldmeyer, M., 2011, “A survey of techniques and challenges in underwater localization,” Ocean Engineering 38: 1663-1676
- Tangley, L., 2010, "Bird Habitats Threatened by Oil Spill". National Wildlife. National Wildlife Federation.
- Time-Of-Flights from a Wave Source to Various Receivers,” IEEE Transactions on Robotics and Automation, vol. 17, no.1, 91-94
- Transportation Research Board Special Report 322, 2016, “Application of Remote Real-Time Monitoring to Offshore Oil and gas operation”, The National Academics Press, ISBN 978-0-309-44242-8 | DOI 10.17226/23499
- Ttojanovic, M., 2006, “On the relationship between capacity and distance in an underwater acoustic communication channel,” Proceedings of the ACM International Workshop on Underwater Networks
- United States Coast Guard, National Response Teams (U.S.), 2011, “On Scene Coordinator Report on Deepwater Horizon Oil Spill “, U.S. Department of Homeland Security, U.S. Coast Guard, 2011 Pages 222.
- Urick, R.J., 1983, “Principles of Underwater Sound”, New York: McGraw-Hill. 3rd ed.
- Wilcock, W.S.D., K.M. Stafford, R.K. Andrew, and R.I. Odom, 2014, “Sounds in the ocean at 1-110 Hz”, Annu. Rev. Mar. Sci., 6:117–40.

[1] http://jeffreyguido.com/work/tdoa_page.html#solution

[2] K. W. Cheung, H. C. So, W. -. Ma and Y. T. Chan, "Least squares algorithms for time-of-arrival-based mobile location," in IEEE Transactions on Signal Processing, vol. 52, no. 4, pp. 1121-1130, April 2004, doi: 10.1109/TSP.2004.823465.

[3] F. K. W. Chan, H. C. So, J. Zheng and K. W. K. Lui, "Best linear unbiased estimator approach for time-of-arrival based localisation," in IET Signal Processing, vol. 2, no. 2, pp. 156-162, June 2008, doi: 10.1049/iet-spr:20070190.

[4] Fokin, G., Kireev, Al-odhari, A. H. A.: TDOA positioning accuracy performance evaluation for arc sensor configuration. In: 2018 Systems of Signals Generating and Processing in the Field of on Board Communications, Moscow, pp. 1-5 (2018).

[5] Akamatsu, T., Okumura, T., Novarini, N., and Yan, H. Y. (2002). “Empirical refinements applicable to the recording of fish sounds in small tanks,” J. Acoust. Soc. Am. 112(6), 3073–3082.

[6] Novak, A., Bruneau, M., and Lotton, P. (2018). “Small-sized rectangular liquid-filled acoustical tank excitation: A modal approach including leakage through the walls,” Acta Acust. Acust. 104(4), 586–596.

[7] Chardon, G., Nowakowski, T., De Rosny, J., and Daudet, L. (2015). “A blind dereverberation method for narrowband source localization,” IEEE J. Sel. Top. Signal Process. 9(5), 815–824.

[8] Dokmanic´, I., and Vetterli, M. (2012). “Room helps: Acoustic localization with finite elements,” in 2012 IEEE International Conference on Acoustics, Speech and Signal Processing (ICASSP), pp. 2617–2620.

[9] Nowakowski, T., de Rosny, J., and Daudet, L. (2017). “Robust source localization from wavefield separation including prior information,” J. Acoust. Soc. Am. 141(4), 2375–2386.

[10] Novak, A., Bruneau, M., and Lotton, P. (2018). “Small-sized rectangular liquid-filled acoustical tank excitation: A modal approach including leakage through the walls,” Acta Acust. Acust. 104(4), 586–596.

[11] Novak, A., Cisar, P., Bruneau, M., Lotton, P., and Simon, L. (2019). “ Localization of sound-producing fish in a water-filled tank,” J. Acoust. Soc. Am. 146(6), 4842–4850.

[12] Daku, B. L. F., Salt, J. E., and McIntyre, C. M. (1992). “Quality of underwater source localization in a multipath environment,” J. Acoust. Soc. Am. 91(2), 957–964.

[13] Johnson, D. H., and Dudgeon, D. E. (1993). Array Signal Processing: Concepts and Techniques (PTR Prentice Hall, Englewood Cliffs, NJ).

[14] Ralph O, Schmidt. Multiple Emitter Location and signal Parameter Estimation. IEEE Trans. On Antennas and Propagation, March 1986. Vol. 34. No. 3. pp 276-280.

[15] M.Gavish etc. Performance Analysis of the VIA ESPRIT Algorithm. IEE-Proc-F. 1993. Vol. 140(2).

P123~128.
[16] A. Delis and G. Papadopoulos, "Enhanced forward/backward spatial filtering method for DOA estimation of narrowband coherent sources," in IEE Proceedings - Radar, Sonar and Navigation, vol. 143, no. 1, pp. 10-16, Feb. 1996
[17] G. Su, M. Morf. The signal subspace approach for multiple wide-band emitter location[J]. IEEE Transactions on Acoustics, Speech, and Signal Processing, 1983, 31(6) : 1502-1522